

Analysis of the Internal Radial Gradient of Chemical Abundances in Spiral Galaxies from CALIFA

A. F. S. CARDOSO ¹, O. CAVICHA ¹, M. MOLLÁ ² AND L. SÁNCHEZ-MENGUIANO ^{3,4}

¹*Instituto de Física e Química, Universidade Federal de Itajubá
Av. BPS, 1303, 37500-903
Itajubá-MG, Brazil*

²*Departamento de Investigación Básica, CIEMAT
Avda. Complutense 40, E-28040
Madrid, Spain*

³*Universidad de Granada, Departamento de Física Teórica y del Cosmos
Campus Fuente Nueva, Edificio Mecenas, 18071
Granada, Spain*

⁴*Instituto Carlos I de Física Teórica y Computacional
Facultad de Ciencias, 18071
Granada, Spain*

ABSTRACT

The study of chemical evolution is of paramount importance for understanding the galaxies evolution. Models and observations propose an inside-out mechanism in the formation of spiral galaxy disks implying a negative radial gradient of elemental abundances when represented in logarithmic scale. However, observed chemical abundance gradients, in some instances, deviate from a single linear negative straight line, revealing inner drops or outer flattenings, particularly in more massive galaxies. This study analyzes oxygen abundance gradients in spiral galaxies based on observations from the Calar Alto Legacy Integral Field Area (CALIFA) survey. Our focus is specifically on examining oxygen abundance gradient profiles, as obtained with data from HII regions, with a special emphasis on the inner radial gradient. We employ an automated fitting procedure to establish correlations between the physical properties of galaxies and bulges and the presence of these inner drops, seeking for potential explanations for these gradient variations. We find that the different criteria used in the literature to distinguish HII regions from other ionization sources in the galaxy, such as Active Galactic Nuclei, significantly impact the results, potentially altering abundance gradient profiles and uncovering galaxies with distinct inner drops. Additionally, we analyze the abundance radial gradients to investigate the impact of diffuse ionized gas (DIG) decontamination on oxygen abundances over the featuring inner drops. We observe that DIG, concentrated mainly in the central regions of galaxies, can modify oxygen abundance gradient profiles if left unaddressed.

Keywords: Chemical abundances — Galaxy abundances — Galaxy bulges — Galaxy disks — Galaxy chemical evolution — HII regions

1. INTRODUCTION

The study of the chemical evolution of spiral galaxies has become extremely important for our understanding of the formation and evolution of galaxies. The chemical abundance gradient is defined as the variation of the

abundance of a certain chemical element as a function of the distance to the center of the galaxy. This measure provides information of the chemical enrichment along galactic disks. Observations and analyses of chemical abundance gradients have confirmed the presence of negative gradients across the disks of spiral galaxies, in agreement with the inside-out model proposed by [Lacey & Fall \(1985\)](#); [Matteucci & Franco \(1989\)](#). According to this model, it is expected a more intense and ear-

lier star formation in the central regions of the galaxies than in the outer ones, indicating that the central regions of the galaxy formed first, or that there was a greater amount of gas available for star formation there.

The abundance gradients in spiral galaxies can be obtained from HII regions, which provide information about the current chemical enrichment in the galaxy (Peimbert & Costero 1969; Searle 1971; Pagel et al. 1992; Martin & Roy 1994; Vilchez & Esteban 1996a; Stasińska et al. 2006; Izotov et al. 2006; Sánchez et al. 2014; Ho et al. 2015; Berg et al. 2020; Zurita et al. 2021; Méndez-Delgado et al. 2022, and many others). Through the observation of their nebular emission lines, they provide valuable information about the chemical composition of spiral galaxies, with oxygen serving as a proxy for gas metallicity (Aller 1984; Osterbrock & Ferland 2006). However, the heating of the gas in the galaxy and their corresponding nebular emission lines, could be attributed to various ionization sources, such as young OB-type stars associated with star-forming regions or Active Galactic Nuclei (AGNs) (Kewley et al. 2006). Additionally, other sources can also ionize the gas, generating the so-called Diffuse Ionized Gas (DIG), located in regions with different properties, such as low densities and high electron temperatures, than the HII regions, but which can be erroneously classified as those ones. The sources that ionize the DIG can be hot low-mass evolved stars (HOLMES) (e.g., Stasińska et al. 2008; Flores-Fajardo et al. 2011; Cid Fernandes et al. 2011), shocks (Collins & Rand 2001), or cosmic rays (Reynolds et al. 2001).

In later-type galaxies (Sb or later), there are evidences that the DIG is concentrated in their central regions (Lacerda et al. 2018, hereafter LA18), located within $R < 1 \text{ HLR}^1$, where R is the distance to the galaxy center. According to LA18, the identification of the DIG in the central regions of galaxies is interpreted as a higher proportion of old stellar populations in galactic bulges. Since AGNs can be potentially another source of ionization of the gas at the inner regions of the spiral galaxies, these regions are more likely to be contaminated by other ionization sources than star-formation (Sánchez et al. 2012). Several models have been proposed in the literature to distinguish between these different ionization sources. In this paper, we will discuss the DIG, addressing the criterion of LA18, who used the equivalent width of $\text{H}\alpha$ ($\text{EW}(\text{H}\alpha)$) to analyze the DIG in CALIFA galaxies. Additionally, we will address the BPT dia-

gram, proposed by Baldwin et al. (1981); the WHAN diagram, developed by Cid Fernandes et al. (2011); as well as the criterion for selecting HII regions presented by Sánchez et al. (2014), which considers the luminosity fraction of young stars.

In the past, several authors have studied abundance gradients in the disks of the spiral galaxies and have found that the slope of the abundance gradients is related to galaxy properties, such as (i) the presence of a bar, where non-barred galaxies also show steeper gradient slopes (e.g., Zaritsky et al. 1994; Roy 1996); (ii) the morphology, where late-type galaxies exhibit steeper slopes (e.g., McCall et al. 1985; Vila-Costas & Edmunds 1992); and (iii) the mass, where less massive galaxies show steeper gradient slopes (e.g., Zaritsky et al. 1994; Martin & Roy 1994; Garnett 1998). However, the development of integral field spectroscopic (IFS) techniques has enabled a more comprehensive study of the spatial abundances distribution in galaxies. The use of IFS in HII regions has allowed for the investigation of extensive samples of galaxies, providing statistically robust results, as this technique enables spectroscopic analysis in two spatial dimensions. On the other hand, the determination of abundance gradients from IFS studies have thus far relied on strong-line abundance calibrations and, therefore, have systematic uncertainties (e.g. Kewley & Ellison 2008; Bresolin et al. 2009a; Maiolino & Mannucci 2019).

In this regard, the CALIFA survey (Sánchez et al. 2012) was a collaboration aimed at acquiring spectroscopic information from galaxies using Integral Field Units (IFU), which enabled the collection of a wide range of data, including morphological type, color, and mass of galaxies, generating two-dimensional maps addressing these features. CALIFA data allows the analysis of ionized gas distribution, chemical abundances, excitation mechanisms, as well as information related to stellar populations, such as their ages and metallicities, and kinematic properties of both the stellar component and ionized gas (Sánchez et al. 2012). Using IFS data, Sánchez et al. (2012) and Sánchez et al. (2014) identify that spiral galaxies exhibit a characteristic abundance gradient when normalized by the effective radius (r_e), regardless of the morphological type of these galaxies, with the gradients showing a very similar slope for all galaxies of approximately $-0.1 \text{ dex } r_e^{-1}$.

However, the use of a single negative gradient to describe the oxygen abundance radial distribution of spiral galaxies is not always the best fit and there are some observational works reporting deviations from these single negative gradients, especially in more massive spiral galaxies (e.g., Martin & Roy 1995; Vilchez & Esteban

¹ HLR corresponds to the half-light radius, defined as the length of the elliptical aperture along the major axis that contains half of the total flux at 5635 Å (González Delgado et al. 2016).

1996b; Bresolin et al. 2009b, 2012; Sánchez-Menguiano et al. 2016, 2018). In the work from Sánchez-Menguiano et al. (2016, hereafter SM16), the authors identify some galaxies that exhibit a radial distribution of oxygen abundances which become flat or, in some cases, even positive in the radial region beyond $2.0 r_e$, in agreement with previous studies based on individual HII regions (Martin & Roy 1995; Vilchez & Esteban 1996b; Bresolin et al. 2009b, 2012). Several authors have proposed different mechanisms to explain the origin of these outer flattenings, such as radial motions of both gas and stars (Goetz & Koeppen 1992; Ferguson & Clarke 2001; Sellwood & Binney 2002; Minchev & Famaey 2010; Bilitewski & Schönrich 2012; Roškar et al. 2012; Daniel & Wyse 2015); a radial dependence of star formation efficiency at large galactocentric distances (Bresolin et al. 2012; Esteban et al. 2013); satellite accretion and minor mergers (Quillen et al. 2009; Qu et al. 2011; Bird et al. 2012); or a balance between outflows and inflows with the intergalactic medium (Oppenheimer & Davé 2008; Oppenheimer et al. 2010; Davé et al. 2011, 2012). However, the nature of this flattening in the external gradient is still a matter of debate, as it is not clear whether this phenomenon is a common feature in galactic disks. Additionally, SM16 also observe a break in the abundance gradient associated with the innermost region in the most massive galaxies, at approximately $0.5 r_e$, showing an inner drop that had also been observed in previous studies (e.g., Belley & Roy 1992; Rosales-Ortega et al. 2011; Sánchez et al. 2012). These deviations in the gradients in the inner regions do not appear to be related to bar effects, luminosity, or galaxy morphology. Subsequently, Sánchez-Menguiano et al. (2018, hereafter SM18) using data of higher spatial resolution from MUSE confirm the existence of this inner drop in the gradient at $0.5 r_e$ for some spiral galaxies. When the presence of an inner drop is detected, a slightly steepened main gradient is observed, suggesting that radial gas motions may play a significant role in shaping chemical abundance profiles. In both works, SM16 and SM18, no significant differences are found in the gradient slope due to the presence or not of a stellar bar. On the contrary, in a sample of 51 galaxies, both barred and unbarred, Zurita et al. (2021) claim that barred galaxies have shallower gradients than unbarred galaxies for low-luminosity galaxies, but the number of low-luminosity barred galaxies in their sample (7) is low to reach a firm conclusion. Thus, given that the origin of the inner drop in the gradient is still unclear, a more thorough investigation of these internal radial gradients is necessary.

The aim of this paper is, therefore, to conduct a comprehensive and detailed analysis of the internal oxygen abundance gradient in a statistically significant sample of spiral galaxies from CALIFA, using information derived from the HII regions within these galaxies. By applying contemporary statistical tools, we identified potential deviations in abundance gradients automatically and without human supervision, requiring only the radial distributions and abundances of the HII regions of each galaxy, as well as setting a few parameters, for the tool to automatically detect these potential deviations. Then, possible connections will be established between the inner drop in the gradient and the galaxy properties, such as their total mass and bulge mass, as well as different criteria of HII regions selection and DIG decontamination. The study sample consisted of the largest possible number of galaxies classified as spirals (S) in the CALIFA sample, as long as they are not involved in merger or interaction processes and exhibit a suitable inclination for analysis.

The paper is organized as follows. In Section 2, the galaxy sample, bulge parameters determination, HII regions classification and the diffuse ionized gas decontamination are presented. In Section 3, we present the abundance determination and the gradient fitting methodology. In Section 4, the obtained results are presented and in Section 5 the discussion of the results. Finally, the conclusions and outline prospects for future studies are given in Section 6.

2. THE GALAXY SAMPLE AND HII REGIONS SELECTION METHODS

The galaxies included in our sample were obtained from CALIFA DR3 (Sánchez et al. 2016). The final sample of the CALIFA survey covered two different configurations for data acquisition, V500 and V1200, encompassing the wavelength range between 3745-7300 Å and 3400-4750 Å, respectively. This selection was applied to galaxies with an absolute magnitude in the range of $-19 > M_r > -23.1$ (Walcher et al. 2014). In the analysis and generation of data cubes, only spaxels with S/N greater than 3 were considered, resulting in a final spectral resolution of approximately 6.5 Å in FWHM and an average spatial resolution of about 1 kpc for galaxies with a redshift range between $0.005 < z < 0.03$ (Sánchez et al. 2012; Walcher et al. 2014; Sánchez et al. 2016). Furthermore, we established specific criteria for the selection of our sample of galaxies:

1. Galaxies must be of morphological types ranging from Sa to Sm, including those with bars;

2. These galaxies were not involved in interaction or merging processes – that is, must be classified as isolated (I) in the CALIFA DR3 catalog;
3. The inclination of the galaxies must be smaller than 65° to avoid uncertainties arising from inclination effect;
4. A minimum requirement of 10 HII regions per galaxy must exist to ensure a reliable analysis of the abundance gradient.

The choice to adopt an inclination of $i < 65^\circ$ represents an intermediate criterion, compared to the studies of SM16 and SM18, which employed inclinations of $i < 60^\circ$ and $i < 70^\circ$, respectively, also with the aim of avoiding the uncertainties arising from the inclination effect. The effective radii were provided by Dr. S. Sánchez (private communication) and correspond to results by Walcher et al. (2014). Based on the conditions established above, we selected a total of 147 spiral galaxies. Detailed information about the main characteristics of these galaxies is available in Table 1.

We used the catalog of multi-component two-dimensional photometric decomposition of galaxies conducted by Méndez-Abreu et al. (2017) to determine the bulge parameters. This catalog comprises a total of 404 galaxies from CALIFA and provides information on the disk, bar, central source, and bulge, such as the effective radius and surface brightness at the effective radius of the bulge. We adopted the effective radius of the bulge in the g -band, which coincides with the wavelength range observed by CALIFA, to determine the bulge mass, following Beifiori et al. (2012):

$$M_{\text{bulge}} = \frac{\alpha r_{e,\text{bulge}} \sigma_{e,\text{bulge}}^2}{G}, \quad (1)$$

where G represents the gravitational constant, $\sigma_{e,\text{bulge}}$ is the velocity dispersion within the effective radius $r_{e,\text{bulge}}$, and α is a parameter related to the Sérsic index that takes into account the galaxy structure. The parameter α can be obtained through a relationship derived by Prugniel & Simien (1997) between α and the Sérsic index. To determine the velocity dispersion at the effective radius of the bulge $\sigma_{e,\text{bulge}}$, we followed Sani et al. (2011) through the expression:

$$\log(r_{e,\text{bulge}}) = 1.55 \log(\sigma_{e,\text{bulge}}) - 0.89 \log(\langle I_{e,\text{bulge}} \rangle) - 9.89, \quad (2)$$

where $\langle I_{e,\text{bulge}} \rangle$ is the surface brightness at the effective radius of the bulge in units of solar luminosity. The conversion from $\langle I_{e,\text{bulge}} \rangle$ from the surface brightness at

the effective radius of the bulge in terms of magnitude ($\mu_{e,\text{bulge}}$) was done (Binney & Merrifield 1998) with:

$$\mu_e [\text{mag}/''^2] = 21.572 + M_{\odot,g} - 2.5 \log(\langle I_e \rangle [L_{\odot}/\text{pc}^2]), \quad (3)$$

where $M_{\odot,g} = 5.07$ is the absolute magnitude of the Sun in the g -band. Thus, using $\mu_{e,\text{bulge}}$ from Méndez-Abreu et al. (2017), we determined $\sigma_{e,\text{bulge}}$ for each bulge in each galaxy. Finally, once determined the values of α , together with $r_{e,\text{bulge}}$ and $\sigma_{e,\text{bulge}}$, we estimate the bulge mass of each galaxy from equation 1, whose results are available in Table 1. It is important to note that some parameters of the bulge for 22 galaxies are not available in the catalog of Méndez-Abreu et al. (2017), making impossible to estimate the bulge mass for these galaxies. These cases are identified by the symbol “.” in Table 1.

Considering the criteria described above, our sample is initially composed of galaxies with masses between $10^{9.07}$ and $10^{11.30} M_{\odot}$, and effective radii between $2.24 < r_e < 17.77$ kpc. The stellar mass is provided by CALIFA and was derived from the growth curve magnitudes using the methods described in Walcher et al. (2008). We have to stress that this is the largest sample employed in the study of radial gradient using IFS data so far. The top panels of Figure 1 illustrates the distribution of the galaxies from our sample in terms of mass, morphological type, and effective radius, distinguishing between barred (B), non-barred (A), and those classified as intermediate (AB). The B, A, and AB classifications are provided by the CALIFA survey itself and were obtained through human visual inspection, as described in Walcher et al. (2014), where five authors classified all the galaxies in the sample as B for barred, A for non-barred, and AB if there was uncertainty. Since SM16 also used CALIFA data in the study of oxygen abundance radial gradients in a sample of 122 galaxies, we made a comparison between some properties of the galaxies in our sample and the sample from that study, shown in bottom panels of Figure 1. From this figure, we can see that the current sample is quite similar to the sample from SM16. However, we can notice that the current sample is composed by a slightly higher fraction of galaxies with large stellar masses and also a slightly higher number of early type spiral galaxies. Moreover, the galaxies from our sample tend to have slightly lower effective radii than those from SM16.

2.1. Criteria for Selecting HII Regions

The CALIFA data are distributed reduced using the technique developed for IFS data reduction in the R3D pipeline (Sánchez 2006). Recently, Espinosa-Ponce et al. (2020) provided a catalog containing the spectroscopic information of clumpy ionized regions detected in 988

Table 1. Fundamental properties of the galaxies in the sample.

Name	RA	DEC	Morph	$\log M_*$	$r_{e,*}$	$\log M_{\text{bulge}}$	$r_{e,\text{bulge}}$	μ_{bulge}	z	Dist	PA	b/a	i
(a)	(b)	(c)	(d)	(e)	(f)	(g)	(h)	(i)	(j)	(k)	(l)	(m)	(n)
IC 0159	01.77	-08.64	SBdm	9.8	5.7	9.2	0.9	21.1	0.013	57	16	0.78	40
IC 0674	11.19	+43.63	SBab	10.9	10.9	9.7	2.1	21.4	0.026	107	125	0.65	50
IC 0776	12.32	+08.86	SAdm	9.3	7.0	8.7	1.4	23.1	0.010	35	85	0.56	56
IC 1151	15.98	+17.44	SBcd	9.8	4.7	8.0	0.3	21.2	0.009	31	39	0.49	61
IC 1256	17.40	+26.49	SABb	10.3	6.0	-	-	-	0.018	66	90	0.59	54

NOTE— The complete Table 1 is available in Appendix A. A portion is shown here for guidance regarding its form and content. The columns of the table correspond to the following identifications: (a) galaxy name; (b) right ascension coordinate in hours; (c) declination coordinate in degrees; (d) morphological type from the Hubble classification, indicating barred galaxies (B), non-barred galaxies (A), and intermediate galaxies that may or may not have a bar (AB); (e) integrated stellar mass of the galaxy in $\log(M_\odot)$; (f) effective radius of the galaxy in units of kpc; (g) mass of the bulge in $\log(M_\odot)$; (h) effective radius of the bulge in units of kpc; (i) surface brightness at the effective radius of the bulge in units of $\text{mag}/''^2$; (j) redshift; (k) galaxy distance in Mpc; (l) position angle of the galaxy disk in degrees; (m) ratio between the semi-minor and semi-major axes of the galaxy; (n) inclination of the galaxy with respect to the line of sight in degrees.

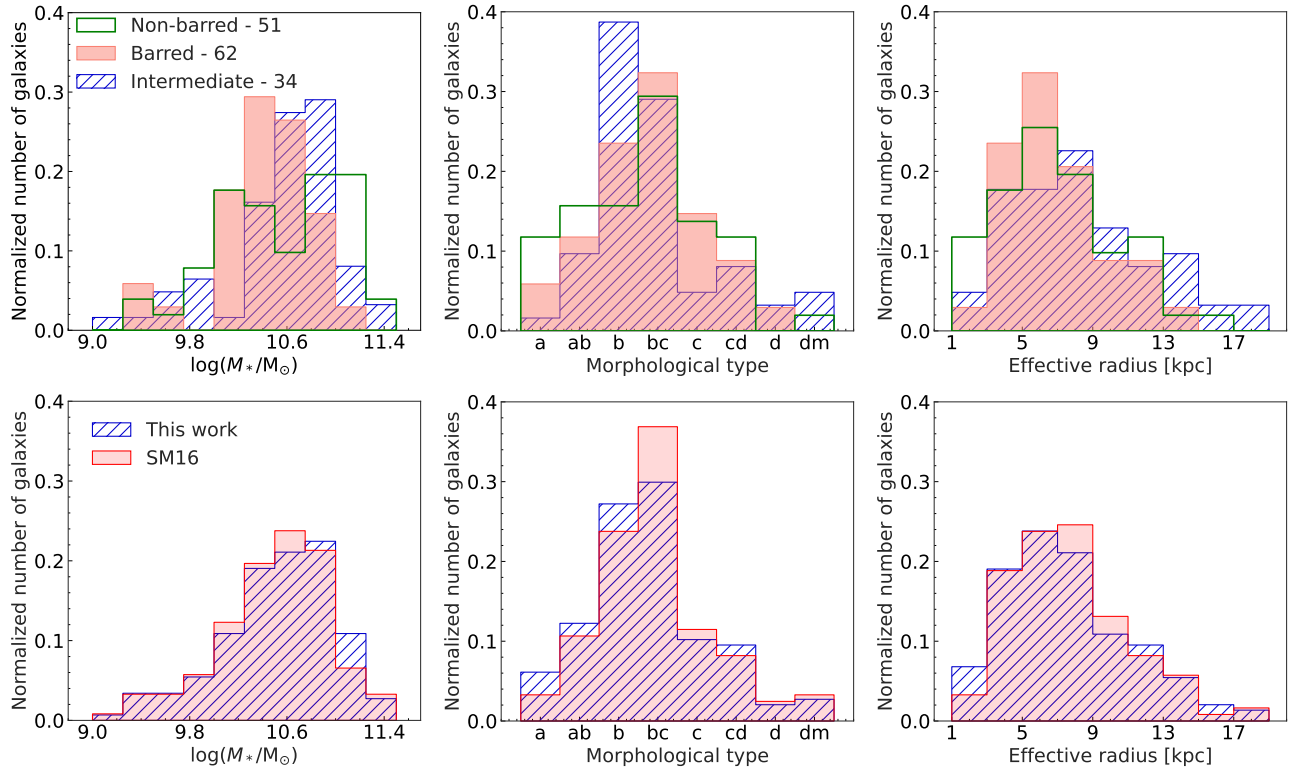


Figure 1. Distribution of properties of galaxies in our sample according to $\log(M_*/M_\odot)$, morphological type, and effective radii r_e , shown in the left, central, and right panels, respectively. The morphological classification in the central panels, from “a” to “dm”, corresponds to spiral galaxies in the Hubble diagram classified as early-type to late-type galaxies, respectively. The top panels show the distribution of the sample galaxies according to the presence or absence of a bar, according to the visual classification described in Walcher et al. (2014). The bottom panels show a comparison between our sample and the sample from SM16, both using CALIFA data.

galaxies observed with CALIFA². For the segregation of HII regions, Espinosa-Ponce et al. (2020) used PYHIIEXPLORER³, a code based on HIIEXPLORER, originally written in Perl (Sánchez et al. 2012). The PYHIIEXPLORER was written in PYTHON, which is a language commonly used in astronomy nowadays, but it essentially performs the same steps as HIIEXPLORER. The detection of ionized regions in PYHIIEXPLORER is based on two initial assumptions: (i) HII regions are isolated structures that have strong emission lines that are clearly above the continuum emission and the average ionized gas emission across each galaxy.; (ii) HII regions have typical sizes on the order of a few hundred parsecs. After this segregation of the HII regions, a FITS file containing the information of the ionized regions is created, making it possible to obtain the emission line fluxes, as well as information about the stellar populations. Further details of the procedures can be found in Espinosa-Ponce et al. (2020).

We have made use of this catalog from Espinosa-Ponce et al. (2020) to obtain the fluxes and $EW(H\alpha)$ of the potential HII regions from the 147 galaxies in our sample. We set limits for the fluxes of the emission lines [OIII], $H\beta$, [NII], and $H\alpha$ from the ionized regions based on a Gaussian distribution, excluding those regions whose error in flux exceeded 3σ of the FWHM from the fitted Gaussian. With these criteria, we obtained a total of 11,410 ionized regions in our sample. For the correction of interstellar extinction, we adopted the theoretical $H\alpha/H\beta$ ratio as 2.86, considering an electron density $n_e = 100 \text{ cm}^{-3}$ and an electron temperature $T_e = 10000 \text{ K}$, following the recombination theory (Osterbrock 1989). The correction in the fluxes were performed as usual and the determination of the $E(B-V)$ is carried out using the extinction curve of Fitzpatrick (1999) as given by the polynomial fit from Cavichia et al. (2010). The mean value and standard deviation of the extinction $E(B-V)$ are 0.21 ± 0.33 , with the first, second, and third quartiles corresponding to 0.06, 0.19, and 0.33, respectively. The physical distances of the ionized regions in galaxies were determined following Scarano et al. (2008) by adopting an intrinsic ellipticity for all galaxies of $q = 0.13$ (Giovanelli et al. 1994).

2.1.1. Diffuse Ionized Gas (DIG)

As explained before, DIG consists of regions with different properties than HII regions, being therefore important to distinguish a HII region from a DIG region.

There are studies in the literature that make this distinction based on the surface brightness of $H\alpha$ (e.g., Zurita et al. 2000; Vogt et al. 2017). However, LA18 argue that using surface brightness of $H\alpha$ is a misleading way to differentiate HII regions from DIG, because if we consider two DIG-dominated regions overlapping along the line of sight, they would together indicate a high surface brightness, causing these DIG-dominated regions be erroneously classified as a single HII region. Therefore, LA18 propose an analysis based on $EW(H\alpha)$ using CALIFA data, defining hDIG by $EW(H\alpha) < 3 \text{ \AA}$ as regions ionized by HOLMES, mDIG by $3 \text{ \AA} < EW(H\alpha) < 14 \text{ \AA}$ as regions ionized by various mixed sources, and SFc by $EW(H\alpha) > 14 \text{ \AA}$ as star-forming complexes⁴.

According to LA18, early-type spiral galaxies show a high concentration of hDIG compared to late-type galaxies. However, they identified that in early-type galaxies the presence of hDIG is more uniformly distributed in their disks, while in later-type galaxies (Sb or later), hDIG is concentrated in the central regions located within $R < 1 \text{ HLR}$, where R is the distance to the galaxy center. The identification of hDIG in the central regions of galaxies is interpreted as a higher proportion of old stellar populations in galactic bulges. It was observed that mDIG can indeed be understood as a mixture of hDIG and SFc since it is primarily located between regions classified as hDIG and SFc.

We performed an analysis of the distribution of ionized regions from the sample, identified as hDIG, mDIG, and SFc, along the radial distribution of galaxies, as shown in Figure 2. We have limited the radial distribution to $r < 2.5 r_e$ for a better visualization. From Figure 2, we observe that only a 2.7% of ionized regions are classified as hDIG and they are predominantly concentrated in the inner regions of galaxies, while SFc tends to move away from the central region and distribute throughout the disk. The mDIG can indeed be understood as a mixture of various sources, as illustrated in Figure 2, as this distribution is concentrated in the intersection between the peaks of hDIG and SFc.

According to Belfiore et al. (2022), the main source of ionization of the DIG proceeds from photons leaking from the HII regions, capable of ionizing the gas across the disks of the galaxies, where they established that the mean free path of these photons is 1.9 kpc. Since the average resolution of CALIFA is approximately 1.0 kpc

² Available in the CALIFA project web page at http://ifs.astroscu.unam.mx/CALIFA/HII_regions/.

³ <https://github.com/cespinosa/pyHIIexplorerV2>

⁴ Regions that contain HII regions, but inevitably mixed with DIG emission in our data. As defined by LA18, SFc are the zones with a larger SF/DIG ratio and are not necessarily dominated by star formation, but simply contain a good proportion of SF-powered line emission.

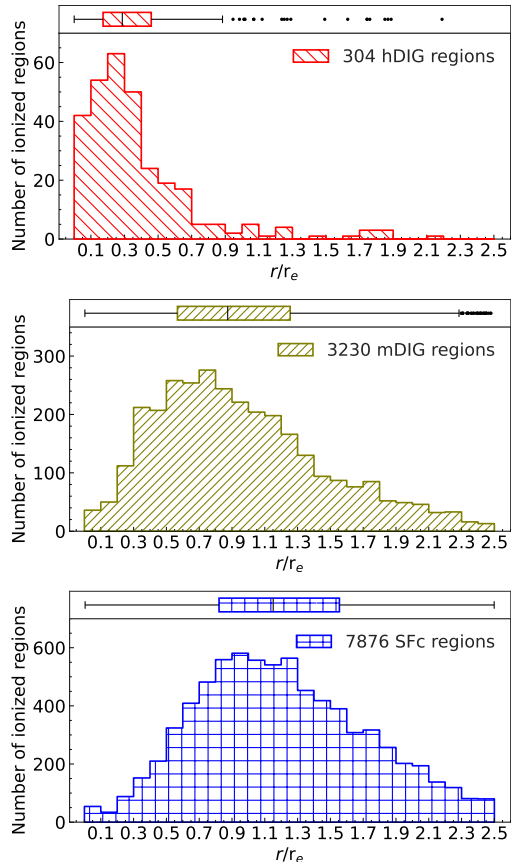


Figure 2. Radial distribution of ionized regions in galaxies, separated into hDIG, mDIG, SFc, as shown in the top, middle, and bottom panels, respectively, indicates the number of ionized regions for each classification. The boxplots provide the median of each classification, as well as the points considered outliers.

(Walcher et al. 2014), and considering that HII regions have sizes on the order of a hundred to several hundreds of parsecs (González Delgado & Pérez 1997; Lopez et al. 2011; Oey et al. 2003), it is not possible to spatially resolve and separate pure HII regions from other potential ionization sources.

To address the effect of DIG, Espinosa-Ponce et al. (2020) develop a method to subtract DIG contamination in regions identified as HII regions in the CALIFA data cubes. This procedure essentially involves identifying spaxels that were not classified as HII regions by PYHIIEXPLORER, calculating the average flux of these spaxels, now referred to as DIG, and subtracting this mean flux from the fluxes of the identified HII regions. Details are available in the work of Espinosa-Ponce et al. (2020).

Therefore, we can also adopt the catalog of Espinosa-Ponce et al. (2020) with the DIG correction, as this cor-

rection is based on spaxels external to those identified by PYHIIEXPLORER in HII regions. As the mean free path of the photons extends beyond these regions, it is reasonable to consider these spaxels as sources ionized by leaked photons. The new initial sample corresponds to the same 147 galaxies, but with the decontamination of the line fluxes performed. Due to our criterion of excluding regions where the line flux errors exceeded 3σ , the new sample contains a slightly smaller number of ionized regions, comprising a total of 10,974 ionized regions. The mean value and standard deviation of the extinction $E(B-V)$ for this sample, excluding DIG contamination, is 0.24 ± 0.43 , with the first, second, and third quartiles corresponding to 0.07, 0.21, and 0.36, respectively.

Here, we analyze both samples to investigate the effect of performing or not performing DIG decontamination. Throughout the paper, we will refer to the first sample as the “with DIG” sample, as the line fluxes in this sample have not undergone DIG decontamination. On the other hand, we will refer to the new sample as the “without DIG” sample, as the line fluxes in this sample have undergone DIG decontamination.

2.1.2. BPT Diagram

In the BPT diagram (Baldwin et al. 1981), different curves are proposed to distinguish HII regions from AGNs. Among the most common ones are those from Kewley et al. (2001, hereafter KE01), which uses theoretical photoionization models; from Kauffmann et al. (2003, hereafter KA03), based on the analysis of integrated spectra from the Sloan Digital Sky Survey (SDSS) galaxies; and from Stasińska et al. (2006, hereafter ST06), using a photoionization model and a power-law-based approach. The region between the curves of KE01 and KA03 remains a subject of debate since, besides other sources of ionization, pure HII regions can be found in this region (Kennicutt et al. 1989; Ho et al. 1997; Pérez-Montero & Contini 2009; Sánchez et al. 2014). Therefore, adopting the curve of KA03 as a criterion to distinguish HII regions from AGNs may exclude known HII regions. However, other studies (Singh et al. 2013; Vogt et al. 2014; Belfiore et al. 2015; Sánchez et al. 2015) have explored other demarcation curves in the BPT diagram in investigating ionization sources, as the exact location of the curve separating HII regions from AGNs is still a matter of controversy (Zinchenko et al. 2016). Figure 3 illustrates the BPT diagram showing the mentioned demarcation curves with the data of our two samples, with and without DIG contamination. The details of the colored diagrams in Figure 3 are discussed in Sections 2.1.1 and 2.1.4. It is noticeable in the

middle panels of the figure that the ionized regions occupy a larger area of the BPT diagram compared with the top panels, even though they are less numerous.

Additionally, bottom panels of Figure 3 also show the BPT diagrams for the sample of HII regions without DIG contamination, with the color code representing the difference in the line fluxes involved in this diagram for the samples with and without DIG contamination. It can be observed that the change in these line fluxes occurs mainly at the edges of the distribution along the BPT diagram. For $[\text{N II}]/\text{H}\alpha$, the greatest difference occurs in the right and left corners of the distribution, while for $[\text{O III}]/\text{H}\beta$, the difference appears in the right corner and the lower region. Furthermore, for the ratio of the line fluxes $[\text{N II}]/\text{H}\alpha$ the difference is less than 10% for 95% of the sample, while for $[\text{O III}]/\text{H}\beta$ the difference is less than 10% for 70% of the sample. These results are in agreement with the change in the density of points between the distribution with and without DIG contamination (upper and central panels), where a slight variation in the density of points along the distribution can be observed.

2.1.3. WHAN Diagram

The WHAN diagram by Cid Fernandes et al. (2011, hereafter CF11), based on the ratio of $[\text{N II}]/\text{H}\alpha$ lines and $\text{EW}(\text{H}\alpha)$, is another widely used diagram to separate HII regions from AGNs and HOLMES. Since the diagram only involves strong emission lines, it suffers of less uncertainties than the traditional diagnostic diagrams like the BPT one, that do rely on weaker lines such as $[\text{O III}]/\text{H}\beta$ and/or $\text{H}\beta$. Figure 4 shows the WHAN diagram from CF11 used for the classification of different ionization sources in our two samples. For the sample with DIG contamination, out of a total of 11,410 ionized regions, there are 304 RGs (passive galaxies or retired galaxies), 9006 SFs (star-forming), 439 wAGNs (weak AGNs), and 1661 sAGNs (strong AGNs). For the sample without DIG contamination, out of a total of 10,974 ionized regions, there are 245 RGs, 8937 SFs, 354 wAGNs, and 1438 sAGNs. We can note that, despite the number of ionized regions being lower in the sample without DIG contamination compared to the sample with DIG contamination, proportionally the sample without DIG has a higher number of regions classified as HII regions, while the number of regions classified as RGs, wAGNs, and sAGNs decreases.

2.1.4. Young Stars Luminosity

Sánchez et al. (2014, hereafter SA14) introduce a different method for the identification of HII regions. Their main criterion is based on the fraction of total luminosity (f_y) in the V band coming from young stars within

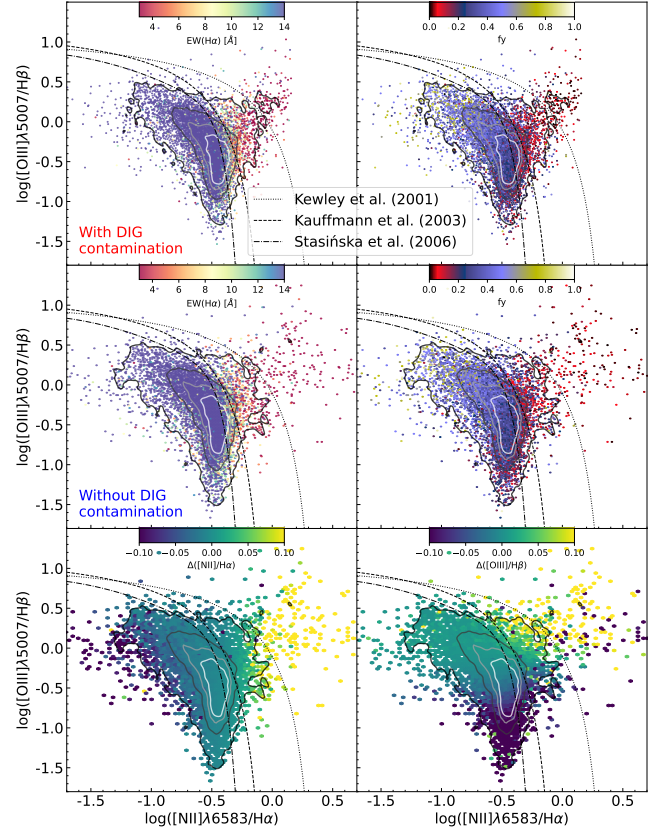


Figure 3. The BPT diagrams of the data samples indicate demarcation curves in the separation between HII regions and AGNs as follows: dashed line: KE01; dash-dotted line: ST06; dotted line: KA03, as shown in the legend. The top panels, identified as with DIG contamination, correspond to the sample of 11,410 ionized regions. The middle panels, identified as without DIG contamination, correspond to the sample of 10,974 ionized regions. In the top and middle left panels the colors correspond to the $\text{EW}(\text{H}\alpha)$ proposed by LA18. In the top and middle right panels the colors correspond to the fraction of young starlight proposed by SA14. The bottom panels show the distribution of the HII regions in the sample without contamination and the color diagrams indicate the difference between the fluxes with and without DIG contamination for $[\text{N II}]/\text{H}\alpha$ (left) and $[\text{O III}]/\text{H}\beta$ (right). In all panels the contours show the density distribution of the HII regions in the samples, where the outermost contour encloses 95% of the regions, and each consecutive contour encloses 75%, 55%, and 35% of the points.

an ionized region, defining young stars as those with an age of less than 500 Myr. The luminosity fraction of the different stellar populations (with different ages and metallicities) is derived through the combination of synthetic Simple Stellar Populations (SSPs) obtained from the modeling of the continuous spectrum of the ionized regions. According to SA14, a simple analysis of the equivalent width of $\text{H}\alpha$ is not sufficient to distinguish between different ionization sources. Figure 3, in the

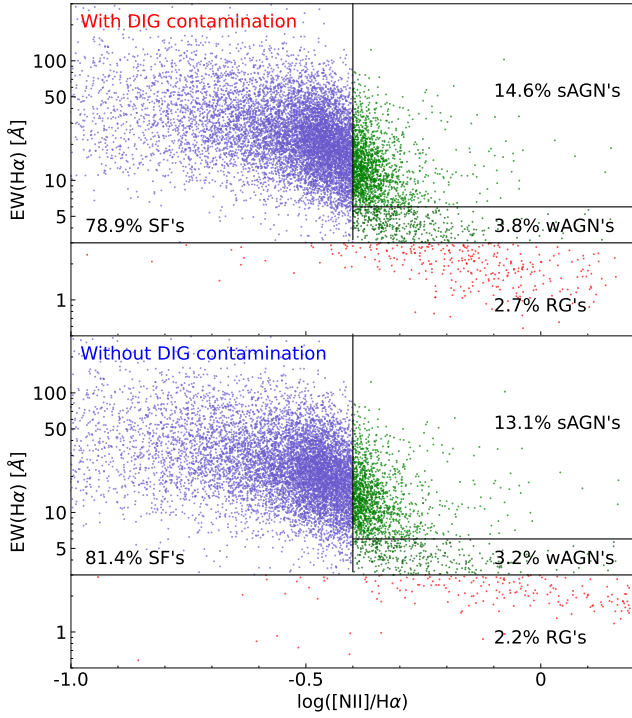


Figure 4. The WHAN diagram from CF11 classifying the ionized regions of the samples with and without DIG contamination is shown in the upper and lower panels, respectively, as indicated in each panel. The percentage of regions classified as SF (star-forming), wAGN (weak AGN), sAGN (strong AGN), and RG (passive galaxy or retired galaxy) for each sample is displayed in each panel.

upper and middle right panels, shows the distribution of ionized regions in the samples with and without DIG contamination, respectively. The fraction of stellar luminosity is indicated with a color diagram, where points closer to the red color, with $f_y < 0.2$, represent regions dominated by old stars, which are not considered HII regions according to the criterion of SA14.

From Figure 3, for the sample with DIG contamination, when we adopt the SA14 criterion, we obtain 8,345 ionized regions with $f_y > 0.2$, corresponding to 73% of ionized regions classified as HII regions. Of this total, 99.8% are located below the KE01 curve. Similarly, for the sample without DIG contamination, when we adopt the SA14 criterion, we obtain 8,156 ionized regions with $f_y > 0.2$, corresponding to 74% of ionized regions classified as HII regions. Of this total, 99.7% are located below the KE01 curve. Therefore, based on the results of SA14, we can conclude that practically all HII regions are located below the curve proposed by KE01, with a contribution of young star luminosity exceeding a 20%.

Table 2 summarizes the number statistics obtained considering or not DIG decontamination and the differ-

Table 2. Number of galaxies and HII regions per criterion.

Criterion	With DIG			Without DIG		
	N_{gal}	N_{HII}	%	N_{gal}	N_{HII}	%
KE01	147	11,252	99	145	10,752	98
KA03	142	10,362	91	141	10,036	91
ST06	130	8,350	73	131	8,364	76
CF11	136	8,965	79	135	8,887	81
SA14	128	8,345	73	128	8,156	74
KE6A	141	10,494	92	141	10,194	93

NOTE—With DIG and Without DIG mean before and after DIG decontamination. KE01: Kewley et al. (2001), KA03: Kauffmann et al. (2003), ST06: Stasińska et al. (2006), CF11: Cid Fernandes et al. (2011), SA14: Sánchez et al. (2014), and KE6A: Kewley et al. (2001) with $\text{EW}(\text{H}\alpha) > 6 \text{ \AA}$.

ent selection criteria to classify the HII regions, showing the percentage of ionized regions classified as HII regions for each criteria from the total of 11,410 and 10,974 HII regions for the samples with DIG and without DIG, respectively.

For the samples with and without DIG contamination, considering the six criteria for selecting HII regions, only 3 galaxies have exactly the requested minimum number of 10 HII regions. However, the distribution of these HII regions extends across the entire galaxy, between $0.5 r_e$ and $2.0 r_e$, ensuring the possibility of obtaining the gradient.

3. ABUNDANCE GRADIENTS

3.1. Abundance determinations

The chemical abundance of ionized gas can be obtained through two main methods: (i) the direct method, based on auroral and nebular line ratios, enabling the determination of temperature and electron density, and consequently, the determination of chemical abundance (e.g. Peimbert & Costero 1969; Stasińska et al. 2006; Pagel et al. 1992; Vilchez & Esteban 1996a; Izotov et al. 2006); (ii) indirect method, also known as the empirical method, based on theoretical models and calibrations that use strong line ratios in determining chemical abundance. The direct method is the most robust way to determine chemical abundances. However, as in the case of HII regions in distant galaxies, these measurements of chemical abundances can be challenging, as the electron temperature decreases with increasing metallicity, making auroral emission lines difficult to measure as they become weak. Therefore, the indirect method should be employed to determine the chemical abundances of these HII regions (Pagel et al. 1979; Pettini & Pagel 2004). The O3N2 index was first introduced

by [Alloin et al. \(1979\)](#) and uses the ratios of strong emission lines $[\text{O III}]/\text{H}\beta$ and $[\text{N II}]/\text{H}\alpha$. These emission lines in the O3N2 indicator are highly sensitive to the oxygen abundance. Moreover, the advantage of using these lines is that they are close in wavelength, providing the benefit of dust extinction correction not being critical in the determination of oxygen abundance. Additionally, as discussed by [Vale Asari et al. \(2019\)](#) and [Kumari et al. \(2019\)](#), the O3N2 index is less affected by DIG compared to other indices proposed in the literature, making it more suitable for estimating oxygen abundance in regions with low spatial resolution. For all these reasons, in this study we will adopt a calibration based on the O3N2 index to derive the oxygen abundances, in particular, the one presented in [Pettini & Pagel \(2004\)](#). We are aware that a more recent calibrator is proposed by [Marino et al. \(2013\)](#), however, as discussed in [Zurita et al. \(2021\)](#), the abundances obtained with the calibrator from [Marino et al. \(2013\)](#) are restricted to a limited range, smaller than the one obtained from the Te-based method for the same regions. This fact motivates the use in this study of the PP04 calibrator instead of the more recent one by [Marino et al. \(2013\)](#) for the O3N2 index.

3.2. Gradient fitting methodology

In some cases, as already explained before, the oxygen abundance radial distributions in spiral galaxies do not strictly follow a straight line and can exhibit variations, including breaks in the main gradient ([Belley & Roy 1992](#); [Rosales-Ortega et al. 2011](#); [Sánchez et al. 2012](#)). As reported in the studies of [SM16](#) and [SM18](#), these radial distributions can take different profiles, such as a single linear gradient, a broken gradient with an inner drop, a broken gradient with an outer flattening, and a doubly broken gradient with an inner drop and an outer flattening.

In the study by [SM16](#), the radial abundance distribution of a large sample of spiral galaxies is investigated, identifying the presence of these deviations from single gradients simply by eye. However, in the study by [SM18](#), an automatic procedure without human supervision is implemented, using functions capable of adjusting the inner drops, similarly to this work, where the selection of the best fit was performed by analyzing the residuals using Monte Carlo simulations and fitting Gaussian distributions of these residuals. Details of this procedure can be found in [SM18](#).

Here we will address this problem of the gradient fitting using a more robust unsupervised automatic fitting procedure that employs a bootstrap process ([Andrae 2010](#)) on the data to escape local minima. In other

words, when identifying a breakpoint in the gradient, the algorithm continues processing the data to find another possible breakpoint, where the gradient better fits the data, resulting in the lowest residual sum of squares (RSS). Thus, the data dispersion may influence the determination of a higher or lower RSS value relative to the fitted profile. To perform the adjustments of the abundance radial gradient, we used the PYTHON package PIECEWISE REGRESSION⁵ developed by [Pilgrim \(2021\)](#), which implements the iterative algorithm from [Muggeo \(2003\)](#) to find breakpoints in the radial distributions. This method simultaneously fits breakpoint positions and the linear models for the different fit segments, and it gives confidence intervals for all the model estimates. The expressions (see below) used are similar to those adopted by [SM18](#), and correspond to the functions that fit the gradients for the case of a single linear profile, for the case where the profile has only one breakpoint, either an inner drop or an outer flattening, and for the case where there can be up to two breakpoints, one inner drop and one outer flattening, respectively:

$$12 + \log(\text{O}/\text{H}) = a_2 r + b, \quad (4)$$

$$12 + \log(\text{O}/\text{H}) = a_1 r + b + (a_2 - a_1)(r - h_1)\mathbf{H}(r - h_1), \quad (5)$$

$$12 + \log(\text{O}/\text{H}) = a_1 r + b + (a_2 - a_1)(r - h_1)\mathbf{H}(r - h_1) + (a_3 - a_2)(r - h_2)\mathbf{H}(r - h_2), \quad (6)$$

where a_1 , a_2 , and a_3 are the coefficients of the internal, main, and external radial gradients, respectively; b is the linear coefficient; h_1 and h_2 are the positions where the inner drop and the outer flattening occur, respectively; and \mathbf{H} is the Heaviside function that ensures the change in the gradient slope in the fit. An example of the fit coefficients is shown in [Figure 5](#) for the galaxy NGC 5016.

For each galaxy, each of the three fits was performed and to ensure the attainment of the global minimum that best fits the data, a two thousand bootstrapped re-sample of the data was implemented, to ensure reliability in the bootstrap confidence limits ([Davison & Hinkley 1997](#)). To determine which of the three fits better captures the data, it is adopted the Akaike Information Criterion (AIC, [Akaike 1973](#)). The AIC, widely used in statistical inference and discussed in [Krishak et al. \(2020\)](#), is recommended for cases where the model must fit a larger number of free parameters, making it suitable for our sample. The AIC is based on a probability

⁵ <https://piecewise-regression.readthedocs.io>

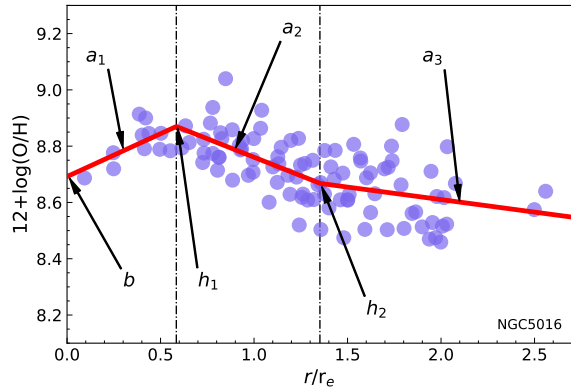


Figure 5. Example of a fit performed using the *piecewise regression* from Pilgrim (2021), illustrating the free parameters of the fit expressed in Equations 4, 5 and 6. The blue dots represent the selected HII regions according to the Kauffmann et al. (2003) criterion, with correction for DIG contamination in the galaxy NGC 5016. The solid red line corresponds to the fit of the oxygen abundance radial distribution. The dashed-dotted lines indicate the positions where the inner drop and the outer flattening occur, respectively.

function, thus providing the probability that a particular model fits the data better than other one according to the model simplicity. In other words, the AIC returns a parameter that compares various fitted models according to their free parameters, and the model with the lowest AIC value has the highest probability of better describing the fitted data. The AIC is calculated as follows:

$$\text{AIC} = 2k - 2 \ln(\mathcal{L}), \quad (7)$$

where k is the number of model parameters and $\ln(\mathcal{L})$ is the maximized log-likelihood of the model, given by:

$$\ln(\mathcal{L}) = -\frac{n}{2} \ln(2\pi) - \frac{n}{2} \ln(\hat{\sigma}^2) - \frac{\text{RSS}}{2\hat{\sigma}^2}, \quad (8)$$

where n is the number of observed data points, $\hat{\sigma}^2 = \text{RSS}/n$ is the variance of the model residual distribution and $\text{RSS} = \sum_{i=1}^n (y_i - \hat{y}_i)^2$ is the residual sum of squares, that is, the sum of squares of the observed data minus the predicted data. Furthermore, according to Narisetty (2020), in cases where the ratio of the number of observed data points to the number of free parameters is less than 40, a correction in determining the AIC is necessary. Therefore, when necessary, this correction was applied, defining the corrected AIC as:

$$\text{AIC}_c = \text{AIC} + \frac{2k(k+1)}{n-k-1}. \quad (9)$$

In the case of a radial distribution with only one break, as suggested by SM18, we considered an inner drop when

the position of this break was limited to the first half of the radial distribution and the slope of the internal gradient was less negative than the slope of the main negative gradient. The other situation in which a break in the gradient occurs was considered as an outer flattening.

4. RESULTS

In Section 4.1, we compare results obtained with different approaches for selecting HII regions, also analyzing how contamination by DIG may affect these results for the oxygen abundance gradient fit. Next, Section 4.2 present the correlations between the physical parameters of galaxies that present an inner drop.

4.1. The Influence of the DIG and the Selection Criteria of H II Regions

As discussed in Section 2.1, several methods are available for selecting star-forming regions in galaxies. We propose to investigate the implications of these criteria and the DIG contamination on the fits of oxygen abundance gradients, as the number of HII regions in the same galaxy can vary significantly depending on the used method in the selection process. Thus, considering the fitting methodology presented in Section 3.2, the fits for the oxygen abundance gradients were performed for all criteria presented in Section 2.1.

Table 3 summarizes the results of this analysis, indicating the frequency of the inner drop for a given galaxy and adopted HII region selection criterion. For each HII region selection criterion, we show in the left the results with DIG contamination (C) and in the right without DIG contamination (D). The column “Galaxy” corresponds to the name of the galaxy. The column “% inner drop” corresponds to the frequency with which a particular galaxy has an inner drop, considering all the six HII region selection criteria, where (C) and (D) also correspond to the samples with and without DIG, respectively. For instance, a galaxy that has an inner drop detected in all the HII region selection criteria after DIG decontamination is marked as 100% in the column “D” inside the “% inner drop” column. The other columns are identified according to the HII region selection criterion discussed in Section 2.1, where “y” indicates the presence of an inner drop, and “n” indicates that there is no inner drop in that criterion. The empty cells in the table, identified by “-”, indicate that there was no occurrence of an inner drop in all of the HII region selection criteria, considering the DIG contaminated and decontaminated samples separately. The rows “ N_{gal} ” and “% $_{\text{gal}}$ ” correspond to the total number of galaxies with an inner drop and the percentage relative to the number of galaxies in each sample.

Table 3. The occurrence of the inner drops.

Galaxy	H II region selection criteria										% inner drop			
	SA14		CF11		KA03		KE01		KE6A		ST06		C	D
	C	D	C	D	C	D	C	D	C	D	C	D		
NGC 7653	y	y	y	y	y	y	y	y	y	y	y	100.0	100.0	
NGC 4047	y	y	y	y	y	y	y	y	y	y	y	100.0	100.0	
NGC 5406	y	n	y	y	y	y	y	y	y	y	y	100.0	83.3	
NGC 0309	y	n	y	y	y	y	y	y	y	y	y	100.0	83.3	
NGC 4210	y	y	y	n	y	y	y	y	y	y	y	100.0	83.3	
NGC 5016	n	n	y	n	y	y	y	y	y	y	n	83.3	50.0	
NGC 3614	n	n	y	y	y	n	y	n	y	n	y	83.3	33.3	
IC 1256	n	n	y	y	y	y	y	y	y	n	y	66.7	83.3	
NGC 5378	n	n	n	n	y	n	y	n	y	n	y	66.7	16.7	
NGC 0776	n	y	n	n	y	y	y	y	y	n	n	50.0	66.7	
NGC 2347	n	n	n	n	y	y	y	y	y	n	y	50.0	66.7	
NGC 5533	y	y	n	y	y	y	n	n	n	n	y	50.0	50.0	
NGC 6004	n	n	y	y	n	y	y	n	y	y	n	50.0	50.0	
NGC 5720	n	n	n	n	y	y	y	y	n	n	y	50.0	33.3	
NGC 4185	n	n	y	y	y	y	n	y	n	y	n	33.3	83.3	
NGC 5056	n	n	n	n	n	n	y	y	y	n	n	33.3	33.3	
NGC 6941	n	n	n	n	y	y	n	n	n	n	y	33.3	33.3	
NGC 7782	n	n	y	n	n	n	y	y	n	n	n	33.3	16.7	
NGC 0214	n	-	n	-	y	-	n	-	n	-	y	33.3	-	
NGC 0257	n	-	y	-	n	-	n	-	n	-	y	33.3	-	
NGC 7631	n	n	n	n	y	y	y	n	n	n	n	33.3	16.7	
NGC 5957	n	n	n	n	y	y	n	y	n	y	n	16.7	66.7	
NGC 1667	n	n	n	y	n	y	n	n	n	n	y	16.7	50.0	
NGC 5267	y	y	n	y	n	n	n	y	n	n	n	16.7	50.0	
NGC 3687	n	y	n	n	n	n	y	y	n	n	n	16.7	33.3	
NGC 4644	n	n	y	y	n	n	n	y	n	n	n	16.7	33.3	
NGC 2805	y	y	n	n	n	n	n	n	n	n	n	16.7	16.7	
NGC 2916	n	n	n	n	n	n	y	y	n	n	n	16.7	16.7	
NGC 7819	n	-	y	-	n	-	n	-	n	-	n	16.7	-	
NGC 5735	n	n	n	n	n	n	y	y	n	n	n	16.7	16.7	
UGC 04195	n	n	n	n	n	n	y	y	n	n	n	16.7	16.7	
MCG-01...	y	-	n	-	n	-	n	-	n	-	n	16.7	-	
NGC 0036	n	-	n	-	n	-	y	-	n	-	n	16.7	-	
NGC 3811	n	-	n	-	n	-	y	-	n	-	n	16.7	-	
NGC 5622	y	-	n	-	n	-	n	-	n	-	n	16.7	-	
NGC 5157	n	-	n	-	n	-	y	-	n	-	n	16.7	-	
NGC 5656	n	-	n	-	n	-	y	-	n	-	n	16.7	-	
NGC 7787	-	n	-	y	-	n	-	n	-	n	-	-	16.7	
NGC 7716	-	n	-	n	-	n	-	y	-	n	-	-	16.7	
NGC 5376	-	n	-	n	-	n	-	n	-	n	-	-	16.7	
NGC 5205	-	y	-	n	-	n	-	n	-	n	-	-	16.7	
N_{gal}	10	9	14	14	18	17	24	22	13	13	14	12	37	32
$\%_{\text{gal}}$	8	7	10	10	13	12	16	15	9	9	11	9	25	22

NOTE— Occurrence of the inner drops for different H II regions selection criteria for the DIG contaminated sample (C, left columns) and for the DIG decontaminated sample (D, right columns).

From the initial sample of 147 galaxies with DIG, 37 galaxies showed an inner drop in at least one of the HII region selection criteria, corresponding to 25% of the sample. On the other hand, for the sample of 147 galaxies without DIG, 32 showed an inner drop in at least one of the criteria, corresponding to 22% of the sample. These numbers are given in the two last rows

of the column “% inner drop” in Table 3. For each H II region selection criterion, the number of galaxies that exhibit an inner drop is also given in the last two rows of Table 3, for both samples.

Considering the sample with DIG contamination, we can see from Table 3 that only 5 galaxies (NGC 7653, NGC 4047, NGC 5406, NGC 0309, NGC 4210) exhibit an inner drop in all HII region selection criteria, corresponding to only 3.4% of the total initial, with only 14 galaxies showing an inner drop in at least three methods (9.5%). It is observed that using the criterion of KE01 results in a higher number of galaxies with an inner drop, while using the criterion of SA14 leads to a lower number of galaxies with an inner drop. This is because this last method excludes more HII regions in the center of the galaxy compared to other methods and, as there are fewer identified HII regions in the inner regions, there is consequently a lower number of galaxies exhibiting the inner drops. For the sample without DIG contamination, only 2 galaxies (NGC 7653, NGC 4047) exhibited an inner drop in all HII region selection criteria, corresponding to 1.4% of the total sample, with only 15 galaxies showing an inner drop in at least three methods (10.2%). Once again, the KE01 criterion presents the highest number of galaxies with an inner drop, while the SA14 criterion presents the lowest number. Moreover, it is evident that, although the difference is small, the sample without DIG has a larger number of galaxies showing an inner drop in at least three of the HII region selection criteria.

The results presented above show that the radial profile of oxygen abundances may vary depending on the adopted criterion to select HII regions, regardless of whether the sample is contaminated by DIG or not. In Figure 6, the fittings for each criterion in three galaxies from the DIG decontaminated sample are presented to illustrate this changing effect on the gradient profile. In the Online Supporting Material (available in the online journal) the fits of the abundance gradients for all HII region selection criteria are shown for the 32 galaxies that present an inner drop in at least one criterion. The galaxy NGC 0309 did not exhibit an inner drop in the SA14 criterion but it does in the other five criteria. When analyzing the position of the inner drop in these last cases, we see that for the CF11, KE01, and KE6A criteria, the positions are practically the same. However, it is possible to notice that the inclinations of the internal radial gradients in these criteria vary considerably. In the KE6A criterion, this gradient is practically flat, while in the KE01 criterion, it is steeper. For the KA03 and ST06 criteria, the positions of the inner drops are closer to the center of the galaxy than in the other cri-

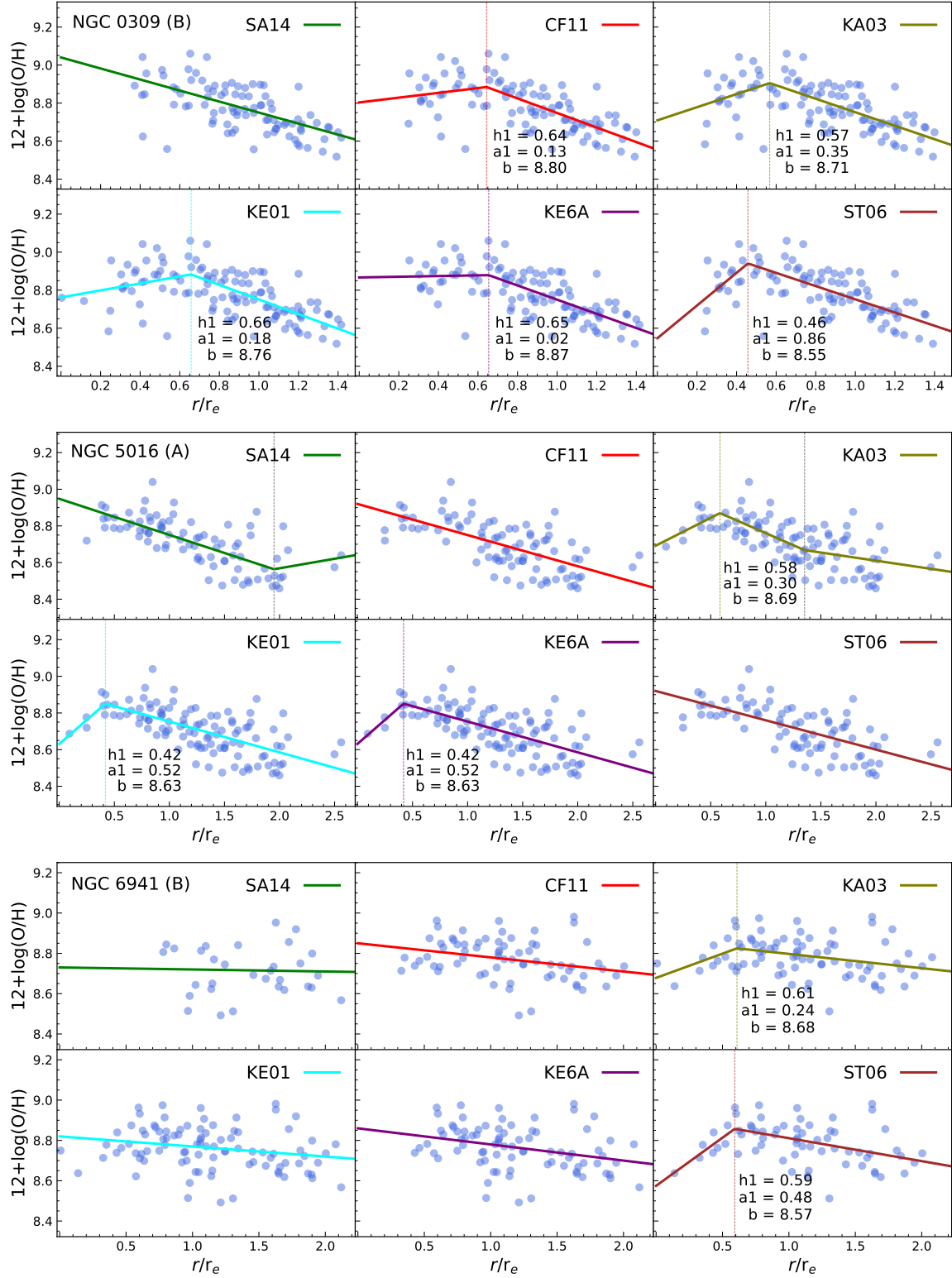


Figure 6. Profiles of abundance gradients without DIG contamination. In each panel in the graphs, the blue points correspond to the HII regions selected by each criterion. The colored solid curve corresponds to the fit of that specific criterion, indicated in the upper right corner of each panel. The dashed line, when present, indicates the position of the inner drop, with the color corresponding to the legend. The gray dashed vertical line, when present, represents the position where the external flattening occurs. The name of each galaxy is presented in the upper left corner of each panel followed by the classification of barred (B), unbarred (A) or intermediate (AB). The complete figure set (11 images) is available in Appendix B.

teria, also presenting steeper internal radial gradients, indicating lower oxygen abundances in the center of the galaxy.

In the case of the galaxy NGC 5016, the presence of the inner drop was identified in the [KA03](#), [KE01](#), and [KE6A](#) criteria, with the [KE01](#) and [KE6A](#) criteria showing the same values for both the positions and inclinations of the radial gradients. However, for the [KA03](#) criterion, the position of the inner drop is different, occurring farther from the center of the galaxy, and it also presents a less steep internal radial gradient, indicating higher abundance in the center of the galaxy. For the galaxy NGC 6941, an inner drop was identified only with the [KA03](#) and [ST06](#) criteria, with the position being quite similar for both of them. However, the internal radial gradient is steeper in the [ST06](#) criterion, indicating a lower oxygen abundance in the inner region of the galaxy. In the case of [KE01](#), the dispersion of the data around the linear fit is higher and the inner drop was not fitted. These results show that both the positions of the inner drop and the profiles of the radial gradients can undergo changes depending on the adopted criteria for HII region selection.

In addition to the method of selecting HII regions influencing the abundance gradient profiles, it is also evident from [Table 3](#) that DIG contamination also influences the profiles, as the number of galaxies present an inner drop varies before and after DIG decontamination, as reported in the last two rows of the table. We can notice that some galaxies that exhibited an inner drop in the sample with DIG contamination no longer show this drop, and vice versa. To assess this effect, we analyzed the gradient profiles of four galaxies, considering the [SA14](#) method for selecting HII regions just to highlight this effect, as shown in [Figure 7](#). We can observe that performing DIG decontamination leads to higher oxygen abundances, especially in the inner regions of the galaxies, within $1 r_e$, which are the regions where an inner drop tends to occur. Furthermore, for some galaxies that previously showed an inner drop before DIG decontamination, they no longer exhibit it, as is the case with NGC 0309 and MCG-01-10-019. We can also observe that NGC 0776 was a galaxy that did not show an inner drop, but after DIG decontamination, it presented an inner drop in the gradient. These effects occur due to the fitting methodology, which also considers the dispersion of data across the entire radial distribution of the galaxy. That is, this slight variation in abundances, although visually minimal, directly impacts the calculation of the RSS of the fitted gradient and, consequently, affects the AIC values of the models. This causes changes in the gradient profiles, altering the

presence or absence of the inner drop. In the case of NGC 0776, it seems that the dispersion is slightly lower and the inner drop is fitted in this case. We should keep in mind that this prevents fitting false drops in the radial distribution.

Regarding NGC 4210, we see that regardless of DIG decontamination, this galaxy showed an inner drop; however, the profile of the inner radial gradient was altered. This effect on the alteration of the inner radial gradient was visually verified in almost all galaxies of the sample and also occurred for all criteria of selecting HII regions.

Another result that can be observed in [Table 3](#) is that the 14 galaxies that exhibit an inner drop in the DIG contaminated and the 15 galaxies from the sample without DIG contamination are not exactly the same. In this way, we conducted a comparison to analyze the number of galaxies exhibiting an inner drop with and without DIG contamination, as shown in [Figure 8](#). We can observe that the criteria of [KE6A](#) and [KA03](#) are the ones that maintained the highest number of galaxies showing an inner drop regardless of DIG correction (highest number of galaxies at the intersection of the diagrams). This can be explained by the fact that using the $EW(H\alpha) > 6 \text{ \AA}$ criterion in the [KE01](#) demarcation curve eliminates HOLMES according to [LA18](#), significantly reducing hDIG. Additionally, as discussed in [Zinchenko et al. \(2019\)](#), [Pilyugin et al. \(2018\)](#) also show that applying the demarcation curve proposed by [KA03](#) eliminates ionized regions that are contaminated by DIG. However, as [Figure 8](#) shows, both criteria do not completely eliminate the ionized regions that are contaminated by DIG.

As it is evident that the presence of DIG directly influences the gradient profiles and the occurrence of the inner drop, the subsequent analysis is based solely on the sample without DIG contamination. For the purpose of comparison, we performed a fit on the sample without DIG contamination according to the calibrators proposed by [Dopita et al. \(2016\)](#) and [Marino et al. \(2013\)](#) for the O3N2 index, as well as the calibrator proposed by [Pettini & Pagel \(2004\)](#) using the N2 index ([Storchi-Bergmann et al. 1994](#)). In the case of the [Dopita et al. \(2016\)](#) calibrator, only 6 galaxies exhibited an inner drop in at least one method of HII region selection, with only 4 galaxies showing an inner drop in at least three criteria. For the [Marino et al. \(2013\)](#), 34 galaxies presented an inner drop with 14 galaxies in at least three criteria. In the case of the [Pettini & Pagel \(2004\)](#) calibrator with the N2 index, 29 galaxies exhibited an inner drop in at least one of the HII region selection cri-

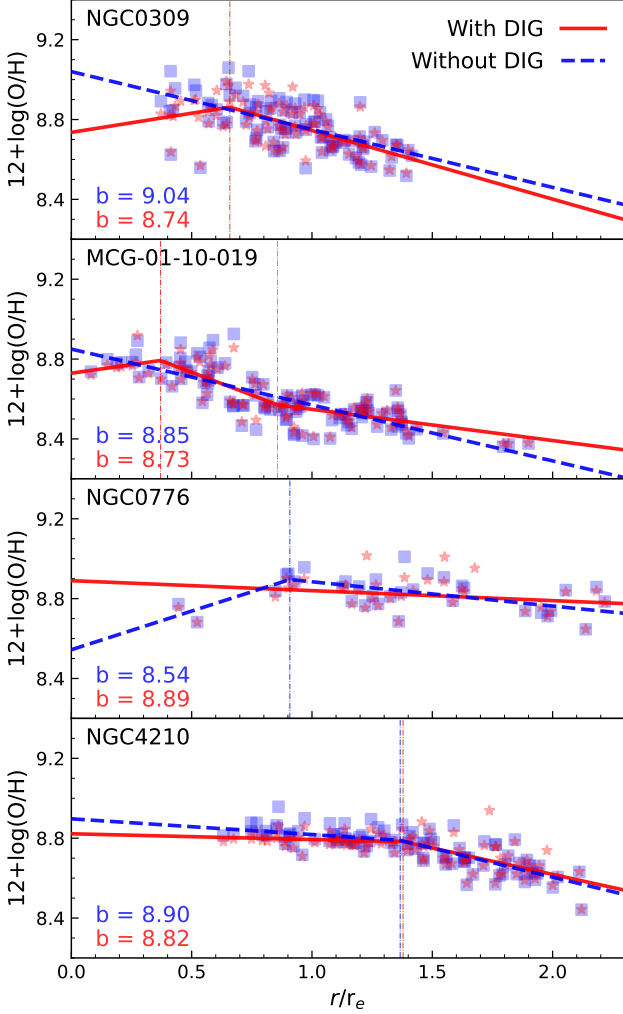


Figure 7. Profiles of oxygen gradients of four galaxies from the sample with and without DIG contamination, represented by red stars and blue squares, respectively. The HII regions were selected according to SA14 criterion. The solid red and dashed blue lines correspond to the fit of the gradient profile for the oxygen abundances derived with and without DIG contamination, respectively. The dash-dotted blue and red vertical lines correspond to the positions of the inner drops. The gray dash-dotted vertical line corresponds to the position of the outer flattening. The abundances at $r = 0$, represented by the value b , are shown in the bottom left corner of each panel.

teria, with 11 galaxies showing an inner drop in at least three criteria.

4.2. The presence of the Inner Drop and the Physical Properties of the Galaxies

Throughout this work we discussed the importance of a careful selection of HII regions in galaxies, noting that the possibility of an inner drop in oxygen abundance gradients may be related to this selection. Therefore, in

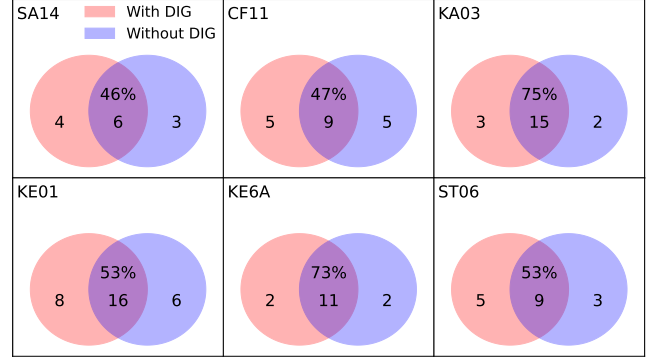


Figure 8. Diagrams depicting the number of galaxies with an inner drop using different HII region selection methods, with and without DIG contamination, differentiated by red and blue colors as indicated in the legend. At the center of each panel is the intersection indicating the percentage of the total number of galaxies with an inner drop relative to the complete set, considering DIG contamination or not.

our next analysis, we restrict the analysis to the galaxies presenting a higher probability of displaying an inner drop according to the different selection criteria, selecting the 15 galaxies that consistently showed an inner drop in at least three criteria after DIG decontamination. This approach aims to ensure greater reliability in identifying galaxies that genuinely exhibit an inner drop. Table 4 displays the coefficients a_1 , a_2 and h_1 for each HII region selection method in the 15 galaxies aforementioned. The two last lines in this table show the mean and the standard deviation for a_1 , a_2 and h_1 for all the galaxies considering the same HII region selection method. We note that the average values for the position of the inner drop converge to $0.8 - 0.9 r_e$, for all the HII region selection criterion. Also, they are higher than the value of $0.5 \pm 0.2 r_e$ from SM18, although they are compatible considering the errors in the measurements. Considering the average standard deviations for h_1 for all the galaxies in a given HII region selection criterion in this table, they are in the range $\sim 0.20 - 0.30 r_e$ and are consistent with the errors in the mean positions obtained in the work of SM18. Additionally, we observe that for KA03 and CF11, the standard deviations have the smallest values, indicating less dispersion in the mean positions of inner drops for these criteria.

The optimal position for the inner drop for each one of the 15 galaxies was determined by calculating the average of positions obtained from the different HII region selection criteria in Table 4, weighted by the individual errors of the coefficients obtained from the fitting procedure. The associated error of the averaged value was determined by propagating the errors from the individual coefficients. The final result can be seen in Table

Table 4. Coefficients a_1 , a_2 and h_1 from profiles of the radial abundance gradients with an inner drop.

Galaxy	HII region selection criteria ^a																	
	SA14			CF11			KA03			KE01			KE6A			ST06		
	a_1	a_2	h_1	a_1	a_2	h_1	a_1	a_2	h_1	a_1	a_2	h_1	a_1	a_2	h_1	a_1	a_2	h_1
NGC 7653	-0.01	-0.15	0.56	-0.08	-0.26	0.91	-0.08	-0.26	0.91	-0.08	-0.25	0.91	-0.09	-0.25	0.92	-0.08	-0.26	0.92
NGC 4047	0.08	-0.24	0.67	0.08	-0.23	0.66	0.08	-0.21	0.64	0.08	-0.21	0.64	0.08	-0.21	0.64	0.08	-0.21	0.64
NGC 5406	–	-0.22	–	0.09	-0.35	1.01	0.10	-0.35	1.01	0.10	-0.35	1.01	0.10	-0.35	1.01	0.10	-0.31	1.00
NGC 0309	–	-0.29	–	0.13	-0.38	0.64	0.35	-0.35	0.57	0.18	-0.38	0.66	0.02	-0.37	0.65	0.86	-0.35	0.46
NGC 4210	-0.08	-0.29	1.37	–	-0.18	–	0.13	-0.22	0.87	0.00	-0.29	1.27	-0.06	-0.29	1.31	-0.04	-0.28	1.30
NGC 5016	–	-0.20	–	–	-0.17	–	0.30	-0.26	0.58	0.52	-0.17	0.42	0.52	-0.17	0.42	–	-0.16	–
IC 1256	–	-0.28	–	0.06	-0.28	0.78	0.04	-0.28	0.81	0.04	-0.28	0.81	0.04	-0.28	0.81	0.06	-0.27	0.79
NGC 0776	0.39	-0.12	0.91	–	-0.13	–	0.12	-0.12	1.03	0.11	-0.12	1.02	0.11	-0.12	1.02	–	-0.11	–
NGC 2347	–	-0.21	–	–	-0.21	–	0.09	-0.28	0.7	0.09	-0.28	0.70	0.09	-0.28	0.70	0.09	-0.28	0.68
NGC 5533	1.55	-0.17	0.34	0.32	-0.20	0.62	0.26	-0.21	0.62	–	-0.02	–	–	-0.17	–	–	-0.12	–
NGC 6004	–	-0.11	–	0.12	-0.17	0.67	0.12	-0.15	0.68	–	-0.09	–	0.08	-0.17	0.75	–	-0.10	–
NGC 4185	–	-0.27	–	0.17	-0.22	0.71	0.16	-0.24	0.72	0.14	-0.24	0.71	0.20	-0.23	0.68	0.16	-0.24	0.73
NGC 5957	–	-0.19	–	0.18	-0.26	1.01	0.21	-0.18	0.87	0.24	-0.17	0.90	-0.04	-0.26	1.19	–	-0.13	–
NGC 1667	–	-0.06	–	0.13	-0.12	0.98	0.04	-0.09	1.17	–	-0.06	–	–	-0.06	–	0.04	-0.14	1.41
NGC 5267	0.21	-0.07	1.28	0.13	-0.09	1.40	–	-0.01	–	0.12	-0.06	1.38	–	-0.02	–	–	-0.03	–
Mean	0.36	-0.19	0.85	0.12	-0.22	0.85	0.14	-0.21	0.80	0.13	-0.20	0.87	0.09	-0.22	0.84	0.14	-0.20	0.88
Std	0.56	0.07	0.37	0.09	0.08	0.23	0.11	0.09	0.18	0.14	0.11	0.26	0.15	0.10	0.24	0.26	0.09	0.29

NOTE—The coefficients a_1 and a_2 are in dex/ r_e and h_1 in r/r_e and are for each HII region selection criterion for galaxies with an inner drop and after DIG decontamination. The last two rows display the mean and standard deviation of the coefficients.

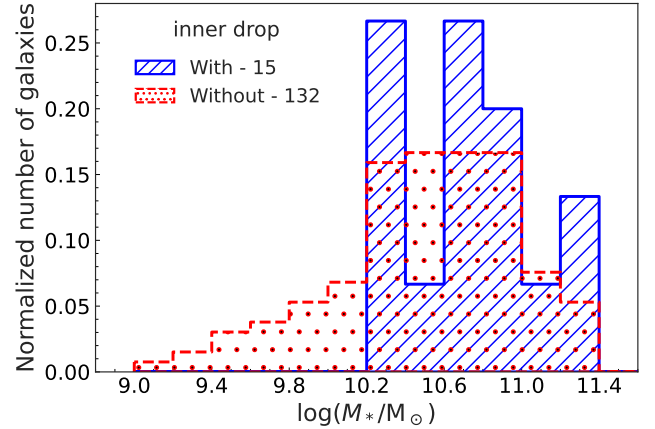
^aAs in Table 2.

Table 5. Average coefficients a_1 , a_2 and h_1 from profiles of the radial gradient in the 15 galaxies that presented an inner drop without DIG contamination.

Galaxy	a_1 (dex/ r_e)	a_2 (dex/ r_e)	h_1 (r/r_e)
NGC 7653	-0.08 ± 0.03	-0.255 ± 0.009	0.90 ± 0.06
NGC 4047	0.08 ± 0.05	-0.218 ± 0.008	0.65 ± 0.05
NGC 5406	0.10 ± 0.09	-0.294 ± 0.032	1.01 ± 0.06
NGC 0309	0.17 ± 0.07	-0.347 ± 0.019	0.55 ± 0.03
NGC 4210	-0.04 ± 0.02	-0.214 ± 0.008	1.19 ± 0.04
NGC 5016	0.40 ± 0.16	-0.173 ± 0.009	0.46 ± 0.06
IC 1256	0.04 ± 0.05	-0.278 ± 0.008	0.80 ± 0.05
NGC 0776	0.13 ± 0.04	-0.119 ± 0.013	0.97 ± 0.06
NGC 2347	0.09 ± 0.06	-0.218 ± 0.007	0.69 ± 0.06
NGC 5533	0.30 ± 0.09	-0.106 ± 0.019	0.45 ± 0.03
NGC 6004	0.09 ± 0.07	-0.115 ± 0.011	0.71 ± 0.07
NGC 4185	0.16 ± 0.04	-0.236 ± 0.016	0.72 ± 0.04
NGC 5957	0.12 ± 0.04	-0.183 ± 0.018	0.95 ± 0.03
NGC 1667	0.05 ± 0.04	-0.074 ± 0.005	1.19 ± 0.13
NGC 5267	0.13 ± 0.04	-0.024 ± 0.006	1.35 ± 0.15

5. In this table we also show the average values for the coefficients a_1 and a_2 for each galaxy. Therefore, all the results presented from now on are based on the mean values of the slopes and positions of the inner drops as given in Table 5.

Similarly to the work from SM16 and SM18, we also identified that the presence of the inner drop occurs in

**Figure 9.** Distribution of the number of galaxies that exhibit an inner drop (in blue) compared to galaxies without an inner drop (in red), considering the 15 galaxies that showed an inner drop in at least three HII region selection criteria, as shown in Table 5.

the most massive galaxies, as can be seen in Figure 9. However, contrary to previous study by SM18, we only identified inner drops in galaxies with $\log(M_*/M_\odot) > 10.2$, that is, the presence of an inner drop in the metallicity gradient is exclusive to the most massive galaxies in our sample.

In the same way, as reported in previous works from SM16; SM18, the inner drops are detected in barred and unbarred galaxies, as seen in Figure 10. In this figure, the top, middle and bottom panels show the relation of the position of the inner drop (h_1), slope of the inner ra-

dial abundance gradient (a_1) and the slope of the main abundance gradient (a_2), with the presence of the bar, respectively. We can observe in the top panel that the average value and the dispersion for the barred galaxies are higher than for unbarred galaxies. We also note that only 4 unbarred galaxies showed an inner drop, while 8 barred galaxies and 3 intermediate galaxies presented the inner drop. It is also possible to observe that barred galaxies exhibit a greater dispersion in the slope of the main negative gradient, while the dispersion in the inner radial gradient is smaller. When the inner drop exists, and considering all the morphological types in Table 5, the main abundance gradient has an average slope of $\langle a_2 \rangle = -0.19 \pm 0.09 \text{ dex } r_e^{-1}$, which is steeper than the value of $-0.08 \pm 0.09 \text{ dex } r_e^{-1}$, for the common radial gradient for spiral galaxies in previous works using CALIFA data (SM16). This result was also noted by previous works from SM16; SM18. The average values and the standard deviations for the slope of the inner radial gradient and the position of the inner drop are $\langle a_1 \rangle = 0.12 \pm 0.11 \text{ dex } r_e^{-1}$, and $\langle h_1 \rangle = 0.84 \pm 0.26 r_e$, respectively.

In an attempt to study possible relationships between the presence of the inner drop and the physical properties of galaxies not yet explored in the literature, as e.g. the physical parameters of the bulges, we conducted analyses using the positions where the inner drop occurs and we also analyzed the slope of the inner radial gradient profile, identified by the coefficients h_1 and a_1 in Figure 5, respectively. Figure 11 shows the relationship between the mean positions of the inner drop and the mean slope of the inner radial abundance gradient with the galaxy and bulge masses and also the bulge effective radius for the 15 galaxies that presented the inner drop without DIG contamination. For all the relations the Pearson correlation coefficient (Pearson 1895) was calculated weighted by the errors of the individual points as given in Table 5. In the case of the position of the inner drop (h_1 (panels a) to c)) the Pearson coefficients point to negative correlations with all the parameters analyzed, although the correlation with the mass of the galaxies is slightly higher.

In Figure 11 panels b) and c) show the relationships between the mass and effective radius of the bulges with the mean positions of the inner drop. For the bulge parameters, the galaxies IC 1256 and NGC 5016 were excluded from the analysis as there is no information on the bulge parameters for these galaxies. A moderate negative correlation between the masses and the effective radii of the bulges with the positions of the inner drop is observed. Therefore, we can expect that a galaxy with an inner drop closer to the center will tend to have

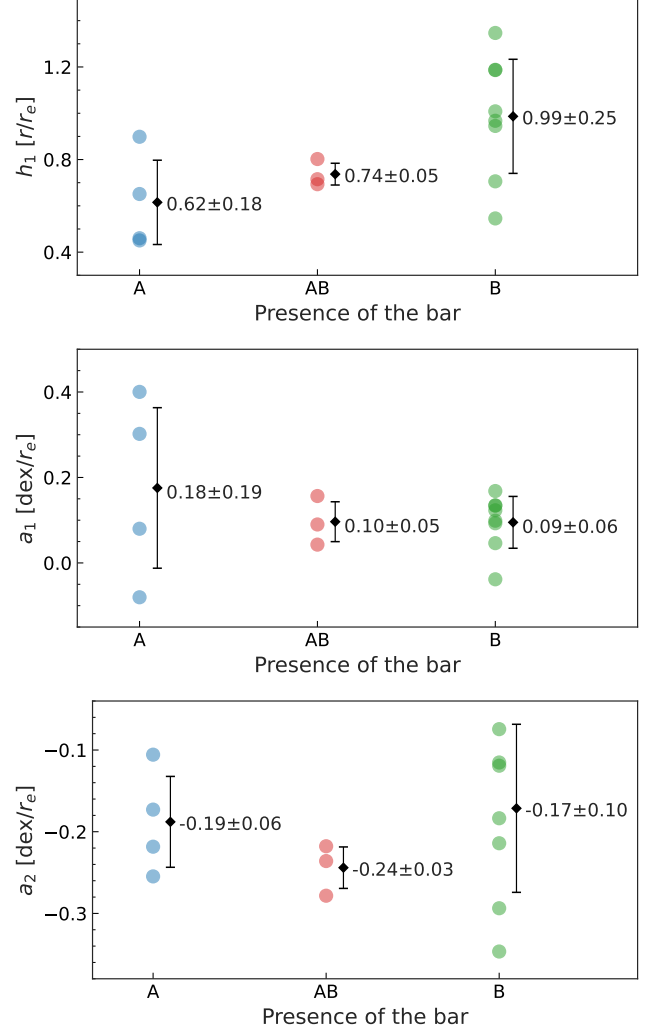


Figure 10. Relation of the coefficients of the fit with the presence or absence of the bar for the 15 galaxies that exhibited an inner drop in at least three methods of selection of HII regions, as shown in Table 5, without DIG contamination. The top, middle, and bottom panels correspond to the position where the inner drop occurs, the coefficient a_1 related to the inner radial gradient, and the coefficient a_2 related to the main negative gradient, respectively. The indices “A”, “AB”, and “B” correspond, respectively, to unbarred galaxies, galaxies that may or may not have bars, and barred galaxies, according to the Hubble classification. For each classification the mean and the standard deviation values are given, and also represented as black diamonds with error bars, respectively.

a more massive bulge, with larger bulge effective radius, and higher surface brightness at the effective radius of the bulge ⁶.

⁶ The effective radii and the surface brightness at the effective radii are correlated following the Kormendy relation (Kormendy 1977).

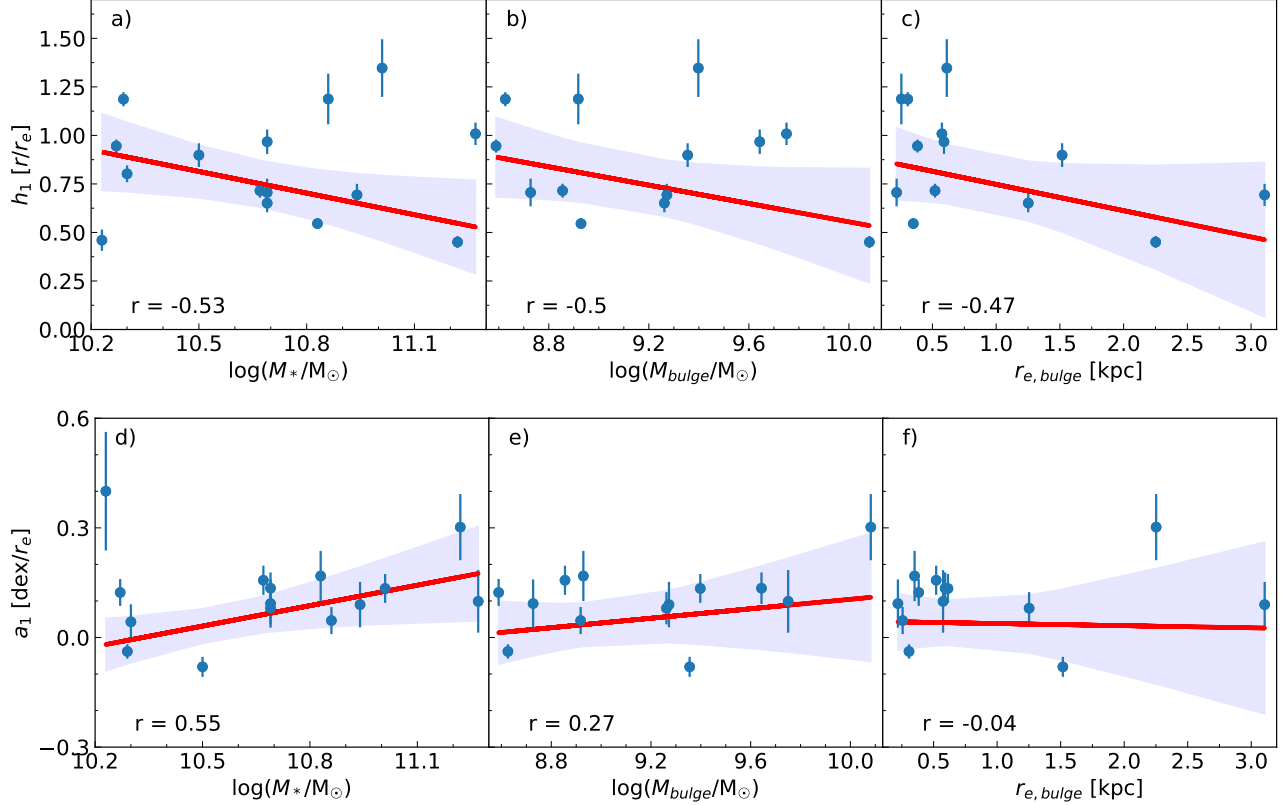


Figure 11. Relationships between the mean position where the inner drop occurs (h_1) with the galaxy and bulge masses and the bulge effective radius presented in panels a) to c). Panels d) to f) show the same relations but for the slope of the inner radial abundance gradient (a_1). The blue points with error bars correspond to the averages values with their respective errors for each galaxy, as given by Table 5. The red continuous lines are the weighted linear fit to the data and the blue shaded areas the 95% confidence interval. The “r” index in the bottom left corner of each panel corresponds to the weighted Pearson correlation coefficient (Pearson 1895).

Figure 11 panels d) to f) show the same relations but for the slope of the inner radial gradient a_1 with the galaxy and bulge masses and the bulge effective radius. In the case of the bulge effective radius, the result pointed to a non-existence of correlation. On the other hand, there are positive correlations with the galaxy and bulge masses, although the first one is stronger. The result that the most massive galaxies tend to have the steepest internal radial gradients was already identified by SM16 and SM18, but now it is quantified in our Figure 11.

5. DISCUSSION

The explanation about the existence of an inner drop in the radial abundance gradient of spiral galaxies is still an unsolved problem. Previous works from SM16; SM18 have made progress on this topic, finding that the average slope of the main radial gradient for O/H of -0.10 ± 0.04 dex/ r_e is slightly steeper than the value of -0.06 ± 0.05 dex/ r_e derived for the galaxies without evidence of this inner drop in the abundances. With

our improved method to fit the abundance gradients, we confirmed this result: -0.19 ± 0.09 dex/ r_e and -0.08 ± 0.04 dex/ r_e for galaxies with and without an inner drop, respectively. SM16; SM18 also find that the galaxies displaying the strongest oxygen abundance inner drop are the most massive ones, suggesting that stellar mass plays a key role in shaping the inner abundance profiles. Our detailed analysis identified a correlation between the slope of the inner drop gradient and the galaxy stellar mass, but we also found that the bulge mass presents a correlation with the slope of the inner radial gradient. Nonetheless, given the present uncertainties in the slope of the inner radial gradient, it is not possible to point which correlation is higher. On the other hand, our analysis pointed that the inner drop occurs exclusively for galaxies with $\log(M_*/M_\odot) > 10.2$.

From the theoretical point of view, the presence of the bar in the galactic center and the associated secular evolution of the disk could be an explanation to the effect of the inner drop in the radial abundance dis-

tribution. Models and simulations show that the non-axisymmetric bar gravitational potential drives gas flow toward the galaxy central region along the bar dust lane (e.g. Fragkoudi et al. 2016, and references therein), and there are observational results confirming bar-driven gas transport (e.g. López-Cobá et al. 2022, and references therein). According to the chemical evolution model (CEM) of the Milky Way by Cavichia et al. (2014), the presence of the bar induces radial gas flows within the corotation radius, being a mechanism for the movement and mixing of gas in barred spiral galaxies, causing the increase of the gas density and decreasing the abundances by dilution and, simultaneously, provoking the possibility of creating new stars, by increasing the star formation rate. Consequently, it is expected the effect of the bar might play an important role in the profiles of abundance gradients. However, as identified in the present work and in those from SM16; SM18, the occurrence of the inner drop was not only associated with the presence of a bar. In spite of that, in our analysis the inner drop in barred galaxies tend to occur at positions furthest from the center in the disk, and also the dispersion of the values is higher. Therefore, there is an evidence that bars can be related with the phenomenon of the inner drop. Although bars are not the only causes of the inner drop, they may amplify it when a bar is present in the central region of the galaxy. From visual inspection of r -band images from SDSS and also from the morphological classifications, we also identified that 12 out of the 15 galaxies (80%) that present an inner drop have some asymmetry in the center, either a bar or a circumnuclear star-forming ring. The possibility that the inversion of the gradient in the central region of spiral galaxies is related with a star-forming ring was also considered in previous works (SM16, and references therein).

Bulges are another important subject of study in spiral galaxies, as they can provide important information regarding chemical abundances in the central region of galaxies. Using a CEM, Cavichia et al. (2023) propose a new model for the formation of the Galactic bulge, where it is formed from inside-out by gas accretion from the halo. The shortest collapse timescales in the central regions of the Galaxy produces a drop of chemical abundances near the bulge-disk interface at ~ 3 kpc (see their figures 5 and 6), similar to the inner drop in the radial abundance gradients in the present work. For the Milky Way, using the average effective radius of 5.07 ± 0.93 kpc from Mollá et al. (2019), the inner drop for the O/H radial abundance gradient is located at $0.6 r_e$ in the work from Cavichia et al. (2023). Thus, a possible relationship between the inner drop and the bulge for-

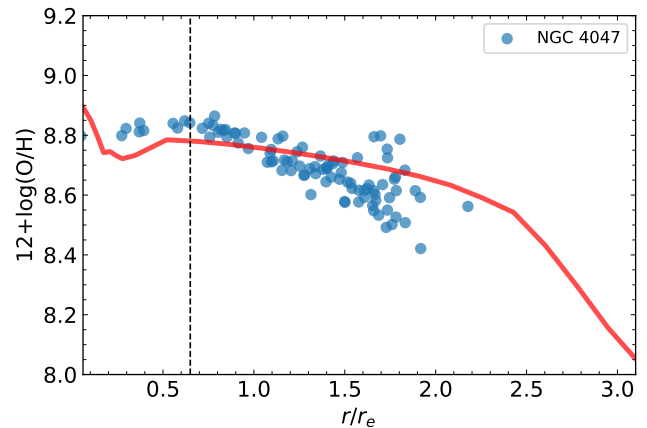


Figure 12. Oxygen abundance radial profile for NGC 4047 (blue filled circles) obtained using KA03 H II region selection method. The dashed vertical line marks the position $0.64 r/r_e$ where an inner drop is detected for this galaxy. The red continuous line corresponds to preliminary results for the Milky Way CEM from Cavichia et al. (2023) adapted for a galaxy with similar mass to NGC 4047.

mation/evolution may be motivated. For a comparison purpose, in Figure 12 the oxygen radial profile for NGC 4047 – a galaxy that present an inner drop in all the H II region selection method in our analysis – is compared with the results of the CEM from Cavichia et al. (2023) developed for the Milky Way and adapted in this work for a spiral galaxy similar to NGC 4047, with virial mass $\log(M_{\text{vir}}) = 11.89$, which corresponds to a stellar mass $M_* = 10^{10.68} M_{\odot}$, and an efficiency $N = 5$ for an Sbc spiral galaxy. We refer to Cavichia et al. (2023) and references therein for more details about the CEM. The CEM presents a drop near the bulge-disk interface because the timescales for the bulge and disk are different in the model, as a result of the inside-out formation of the bulge. Although the result is still preliminary, the model is promising in explaining the inner drop in the chemical abundances radial profiles of the spiral galaxies. To confirm this we need observations with higher spatial resolution to obtain data for $r < 0.5 r_e$ for a larger number of galaxies. However we should note that these are still preliminary results and detailed CEM for spiral galaxies with different masses will be published in a forthcoming work.

Our analysis pointed to a negative correlation between the position of the inner drop and the masses and effective radii of the bulges. Thus, the higher the values of these parameters, the lower the positions where the inner drops occur. The stellar masses of the galaxies may as well as be correlated with the positions of the inner drops, given the uncertainties in the determination of the parameters.

Considering the DIG contamination and all the six different criteria for selecting HII regions, it is evident that, in some cases, the change in the gradient profile experiences a considerable alteration depending on the criterion. In addition to DIG influencing the profile of the radial gradients, we verified that the choice of different methods for selecting HII regions changes the profile of the oxygen abundance distribution, as can be seen in Figure 6, where the fits of the abundance gradients for all HII region selection criteria are shown for the 32 galaxies that present an inner drop in at least one criterion with this new sample. In some cases, the method to select HII regions removed the data in the inner regions of the galaxies and the radial distribution of abundances could not be characterized in these central regions. On the other hand, there were situations where the radial distribution of the chemical abundances along the disk changed, depending on the HII regions selection method, increasing the dispersion of the data and the inner drop, that was detected in a different method, was not detected anymore. It is also clear from the analysis presented in Section 4.1 that the presence of the inner drop was also sensitive on the adopted method to derive the abundances. In the case of the [Dopita et al. \(2016\)](#) calibration based on the H α , N II and S II lines, it was observed the largest difference in the abundance gradient fitting and the detection of the inner drops. On the other hand, the calibrators for the O3N2 index, based on the ratios of strong emission lines [O III]/H β and [N II]/H α from [Pettini & Pagel \(2004\)](#) and [Marino et al. \(2013\)](#), produced similar results, detecting a large number of inner drops in the radial abundance distributions.

In order to draw firmer conclusions about the correlations obtained in this work between the position where the inner drop occurs and the slope of the inner radial O/H gradient, we need to increase the sample of galaxies that present an inner drop in the radial abundance gradient. We also need more observations of the gas motions in the inner regions of the spiral galaxies to better understand the relation of the gas motions and the inner radial abundance gradients.

6. CONCLUSIONS

This study provided a comprehensive investigation of oxygen abundance gradients and, consequently, star-forming regions in galaxies, employing different methods for the selection of the HII regions. The results obtained highlight the intrinsic complexity of the chemical evolution of galaxies.

One of the most significant findings was the sensitivity of abundance gradients to different criteria for selecting

HII regions. It was observed that the choice of a specific method can lead to substantial variations in the profiles of abundances, with marked changes in the positions of breaks and the slopes of the gradients in several galaxies. The selection of different methods implies the exclusion of more or fewer HII regions in the inner region, causing the exclusion of these regions to affect the number of galaxies that may exhibit an inner drop. This result highlights the critical importance of adopting robust and consistent criteria when investigating the properties of galaxies.

We also observed that the DIG can impact the results by altering the profile of the gradients. This alteration in the profiles can be more or less significant depending on the selection criteria of HII regions, as shown in Figure 8. In other words, depending on the adopted criterion, galaxies that previously showed an inner drop may no longer present this drop, and vice versa. This may be associated with the determination of oxygen abundance in spaxels which emission might not come exclusively from the HII regions. This may lead to wrong determination of abundances when using a calibrator that is not suitable for determining abundances in regions not strictly ionized by young stars. However, we noted that the criteria of [Kauffmann et al. \(2003\)](#) and [Kewley et al. \(2001\)](#) with $EW(H\alpha) > 6 \text{ \AA}$ for the selection of HII regions stand out for their robustness regarding DIG contamination. As discussed earlier, these two criteria maintained about 70% of the number of galaxies exhibiting a break, regardless of DIG decontamination, despite it being clear that DIG directly affects the distribution irrespective of the adopted criteria.

Another highlight of this study was the observed trend in the relationship between the position of the inner drop and the galaxy stellar mass. Despite the small number of galaxies, the robustness of the adopted criterion, which considered galaxies with breaks in at least three different criteria, ensured the reliability of the observed trend. We found that galaxies that present larger masses tend to have an inner drop closer to the center of the galaxy. Similar relations were also found for the bulges masses and effective radii, although the correlations were slightly weaker. In other words, the inner drop tends to occur closer to the center of the galaxy in galaxies with larger effective bulge radii and, consequently, higher surface brightness at the effective radius of the bulge.

Besides the positions where the inner drops occur, we also analyzed the slope of the inner radial gradient, identified by the coefficient a_1 . Correlations were also identified between the slope of the inner radial gradient and the galaxy stellar mass and the mass of the bulge, where

more massive galaxies and more massive bulges tend to present steeper inner radial gradients.

A more robust approach to clarify the obtained results involves acquiring data with higher spatial resolution, aiming to more effectively eliminate DIG contamination. Additionally, investigating the radial velocities of gas in galaxies can provide clues about the presence of inner drops, as the gas radial movements have the potential to cause significant changes in the distribution of gas clouds. Therefore, obtaining data with high spatial resolution becomes crucial, allowing for the effective and reliable distinction and separation of star-forming regions from regions ionized by different types of sources. This is essential for deepening the study of chemical abundance gradients.

We thank the anonymous referee for their suggestions, which improved this paper.

AFSC acknowledges the scholarship from FAPEMIG. OC acknowledges funding support from FAPEMIG grant APQ-00915-18. OC and MM have been funded through grants PID2019-107408GB-C41 and PID2022-136598NB-C33 by MCIN/AEI/10.13039/501100011033 and by “ERDF A way of making Europe”.

This study uses data provided by the CALIFA survey (<http://califa.caha.es/>); it is based on observations collected at the Centro Astronómico Hispano Alemán (CAHA) at Calar Alto, operated jointly by the Max-Planck-Institut für Astronomie and the Instituto de Astrofísica de Andalucía (CSIC).

This work has made use of the computing facilities available at the Laboratory of Computational Astrophysics of the Universidade Federal de Itajubá (LAC-UNIFEI). The LAC-UNIFEI is maintained with grants from CAPES, CNPq and FAPEMIG.

APPENDIX

A. GENERAL PROPERTIES OF SAMPLE GALAXIES

Table 1 below contains information on the main properties of the galaxies and bulges in the sample. The columns of the table correspond to the following identifications: (a) galaxy name; (b) right ascension coordinate in hours; (c) declination coordinate in degrees; (d) morphological type from the Hubble classification, indicating barred galaxies (B), non-barred galaxies (A), and intermediate galaxies that may or may not have a bar (AB); (e) integrated stellar mass of the galaxy in $\log(M_{\odot})$; (f) effective radius of the galaxy in units of kpc; (g) mass of the bulge in $\log(M_{\odot})$; (h) effective radius of the bulge in units of kpc; (i) surface brightness at the effective radius of the bulge in units of mag''^{-2} ; (j) redshift; (k) galaxy distance in Mpc; (l) position angle of the galaxy disk in degrees; (m) ratio between the semi-minor and semi-major axes of the galaxy; (n) inclination of the galaxy with respect to the line of sight in degrees.

Table A1. Fundamental properties of the galaxies in the sample.

Name	R.A.	Decl.	Morph	$\log(M_*)$	$r_{e,*}$	$\log(M_{\text{bulge}})$	$r_{e,\text{bulge}}$	μ_{bulge}	z	Dist	PA	b/a	i
(a)	(b)	(c)	(d)	(M_{\odot})	(kpc)	(M_{\odot})	(kpc)	($\text{mag}/''^2$)	(j)	(Mpc)	(deg)	(m)	(deg)
IC 0159	01.77	-08.64	SBdm	9.8	5.7	9.2	0.9	21.1	0.013	57	16	0.78	40
IC 0674	11.19	+43.63	SBab	10.9	10.9	9.7	2.1	21.4	0.026	107	125	0.65	50
IC 0776	12.32	+08.86	SAdm	9.3	7.0	8.7	1.4	23.1	0.010	35	85	0.56	56
IC 1151	15.98	+17.44	SBcd	9.8	4.7	8.1	0.3	21.2	0.009	31	39	0.49	61
IC 1256	17.40	+26.49	SABb	10.3	6.0	-	-	-	0.018	66	90	0.59	54
IC 1683	01.38	+34.44	SABb	10.6	5.0	9.4	0.4	19.0	0.016	71	-14	0.59	54
IC 4566	15.61	+43.54	SBb	10.9	9.1	9.3	0.5	19.7	0.021	80	148	0.69	47
IC 5309	23.32	+08.11	SABc	10.3	3.5	9.4	1.4	21.8	0.014	57	21	0.49	61
MCG-01-10-019	03.68	-06.42	SABbc	10.2	12.4	9.2	1.1	21.4	0.017	75	12	0.58	55
NGC 0001	00.12	+27.71	SAbc	10.8	6.2	9.9	2.2	21.3	0.015	66	108	0.80	37
NGC 0036	00.19	+06.39	SBb	10.9	15.3	9.6	4.1	22.9	0.020	88	77	0.65	50
NGC 0160	00.60	+23.96	SAa	11.0	11.7	10.2	2.3	20.9	0.017	75	49	0.63	52
NGC 0165	00.61	-10.11	SBb	10.6	13.3	9.6	0.8	20.1	0.019	84	88	0.82	35
NGC 0180	00.63	+08.64	SBb	10.9	13.1	9.4	0.6	19.9	0.017	75	159	0.64	51
NGC 0214	00.69	+25.50	SABbc	10.8	6.9	9.3	0.5	19.5	0.015	66	62	0.66	49
NGC 0234	00.73	+14.34	SABc	10.7	6.3	9.2	0.5	20.0	0.015	62	75	0.85	32
NGC 0237	00.72	-00.12	SBc	10.3	4.2	9.4	1.0	21.1	0.014	57	144	0.57	56
NGC 0257	00.80	+08.30	SAc	10.8	8.9	9.6	0.8	20.0	0.017	75	92	0.58	56
NGC 0309	00.95	-09.91	SBcd	10.8	13.5	8.9	0.4	19.7	0.018	80	108	0.84	33
NGC 0447	01.26	+33.07	SBa	11.1	13.8	9.9	1.2	20.2	0.018	80	20	0.60	54
NGC 0477	01.36	+40.49	SABbc	10.5	14.5	9.3	0.8	20.7	0.019	84	-38	0.66	50
NGC 0496	01.39	+33.53	SAcd	10.4	11.4	8.2	0.3	20.5	0.020	88	38	0.58	55
NGC 0570	01.48	-00.95	SBb	11.0	9.0	9.8	1.1	20.2	0.018	80	102	0.70	46
NGC 0681	01.82	-10.43	SABa	10.5	3.7	-	-	-	0.006	22	69	0.65	50
NGC 0716	01.88	+12.71	SABb	10.6	5.8	-	-	-	0.015	66	57	0.64	51
NGC 0768	01.98	+00.53	SBc	10.5	10.9	9.1	2.2	22.8	0.023	102	-65	0.55	57
NGC 0776	02.00	+23.64	SBb	10.7	7.1	9.6	0.6	19.3	0.016	71	141	0.69	47
NGC 0787	02.01	-09.00	SAa	11.0	6.8	9.7	0.7	19.5	0.015	66	81	0.81	37
NGC 0873	02.28	-11.35	SAcd	10.4	4.5	9.1	0.2	18.2	0.013	57	122	0.86	32
NGC 0941	02.47	-01.15	SAcd	9.3	2.8	-	-	-	0.005	22	156	0.87	30
NGC 0991	02.59	-07.15	SABcd	9.6	3.8	-	-	-	0.005	22	85	0.92	23
NGC 1056	02.71	+28.57	SAa	10.0	3.4	-	-	-	0.005	22	-24	0.57	56
NGC 1070	02.72	+04.97	SAb	10.9	7.2	9.2	0.4	19.3	0.013	57	182	0.82	35
NGC 1093	02.80	+34.42	SBbc	10.5	7.4	9.6	1.6	21.5	0.017	75	109	0.62	52
NGC 1094	02.79	-00.29	SABb	10.7	7.8	9.4	0.4	18.9	0.021	93	90	0.71	46
NGC 1659	04.77	-04.79	SABbc	10.5	6.4	9.9	0.2	15.9	0.015	64	45	0.59	55
NGC 1667	04.81	-06.32	SBbc	10.9	5.1	8.9	0.3	19.1	0.015	66	-7	0.64	51
NGC 2253	06.73	+65.21	SBbc	10.5	2.3	9.0	0.2	18.6	0.013	48	137	0.87	30
NGC 2347	07.27	+64.71	SABbc	10.9	5.9	9.3	3.1	23.0	0.015	62	8	0.64	51
NGC 2449	07.79	+26.93	SABab	10.9	5.7	7.7	1.5	25.3	0.017	71	210	0.50	61
NGC 2487	07.97	+25.15	SBb	10.8	11.8	9.2	0.6	20.1	0.017	71	42	0.67	48
NGC 2530	08.13	+17.82	SABd	10.2	9.2	9.0	0.8	20.9	0.017	71	107	0.80	38
NGC 2540	08.21	+26.36	SBbc	10.5	7.9	-	-	-	0.022	89	131	0.71	45
NGC 2543	08.22	+36.25	SBbc	10.3	9.5	8.9	0.3	19.1	0.009	39	48	0.60	54

Continues on the next page

Table A1 – *Continuation*

Name	R.A.	Decl.	Morph	$\log(M_*)$	$r_{e,*}$	$\log(M_{\text{bulge}})$	$r_{e,\text{bulge}}$	μ_{bulge}	z	Dist	PA	b/a	i
(a)	(h)	(deg)	type	(M_{\odot})	(kpc)	(M_{\odot})	(kpc)	(mag/'' ²)	(j)	(Mpc)	(deg)	(m)	(deg)
	(b)	(c)	(d)	(e)	(f)	(g)	(h)	(i)	(j)	(k)	(l)	(m)	(n)
NGC 2558	08.32	+20.51	SABb	10.8	9.1	9.7	0.6	19.3	0.017	75	-21	0.63	51
NGC 2565	08.33	+22.03	SBb	10.7	5.6	9.9	0.4	17.9	0.013	48	-13	0.46	63
NGC 2595	08.46	+21.48	SABc	10.6	12.4	9.9	1.0	20.1	0.015	66	-9	0.70	46
NGC 2604	08.56	+29.54	SBd	9.7	3.7	-	-	-	0.008	31	-9	0.88	29
NGC 2638	08.71	+37.22	SAb	10.8	5.0	-	-	-	0.014	58	64	0.49	62
NGC 2639	08.73	+50.21	SAa	11.2	4.2	9.9	1.0	19.7	0.012	44	-46	0.51	60
NGC 2730	09.04	+16.84	SBcd	10.1	7.0	8.7	0.7	21.7	0.014	53	65	0.64	51
NGC 2805	09.34	+64.10	SAC	10.1	5.8	9.1	2.7	23.7	0.007	22	18	0.76	41
NGC 2906	09.54	+08.44	SABc	10.4	3.0	8.6	0.2	19.1	0.008	31	87	0.51	60
NGC 2916	09.58	+21.71	SABc	10.8	7.3	9.3	0.7	20.3	0.014	53	13	0.59	55
NGC 3057	10.09	+80.29	SBdm	9.1	4.9	-	-	-	0.006	22	182	0.58	55
NGC 3106	10.07	+31.19	SAab	11.2	12.5	9.7	2.5	21.5	0.022	89	141	0.93	22
NGC 3381	10.81	+34.71	SBd	9.7	2.2	7.7	0.1	20.5	0.007	22	48	0.71	46
NGC 3614	11.31	+45.75	SABbc	10.2	7.3	8.3	1.2	23.5	0.009	31	98	0.72	44
NGC 3687	11.47	+29.51	SBb	10.3	3.9	8.5	0.2	19.2	0.010	35	156	0.92	24
NGC 3811	11.69	+47.69	SBbc	10.4	4.6	9.3	0.3	18.4	0.012	44	13	0.62	52
NGC 3994	11.96	+32.28	SABbc	10.4	3.4	9.0	0.3	18.8	0.012	44	9	0.47	63
NGC 4047	12.05	+48.64	SABc	10.7	4.4	9.3	1.3	21.7	0.013	48	99	0.79	38
NGC 4185	12.22	+28.51	SABbc	10.7	8.6	8.9	0.5	20.7	0.015	53	169	0.64	51
NGC 4210	12.25	+65.99	SBb	10.3	3.9	8.6	0.3	20.1	0.011	39	91	0.73	44
NGC 4470	12.49	+07.82	SAC	10.0	2.6	-	-	-	0.009	31	3	0.66	50
NGC 4644	12.71	+55.15	SAb	10.4	6.6	9.1	1.2	21.9	0.018	71	48	0.45	64
NGC 4961	13.10	+27.73	SBcd	9.7	3.1	8.0	0.2	21.1	0.010	35	107	0.66	50
NGC 5000	13.16	+28.91	SBbc	10.7	7.3	8.8	0.5	20.4	0.021	80	82	0.60	53
NGC 5016	13.20	+24.10	SABc	10.2	3.6	-	-	-	0.011	35	58	0.73	44
NGC 5056	13.27	+30.95	SABc	10.5	7.8	8.9	1.1	22.0	0.021	80	180	0.59	55
NGC 5157	13.45	+32.03	SBab	11.2	9.5	10.0	1.6	20.7	0.026	106	129	0.73	44
NGC 5205	13.50	+62.51	SBbc	9.9	2.6	8.3	0.2	19.9	0.007	22	147	0.67	49
NGC 5218	13.54	+62.77	SBab	10.7	3.8	-	-	-	0.011	39	91	0.56	57
NGC 5267	13.68	+38.79	SBab	11.0	8.1	9.4	0.6	19.9	0.022	84	44	0.49	62
NGC 5320	13.84	+41.37	SABbc	10.3	6.3	8.4	0.4	21.3	0.011	35	123	0.55	57
NGC 5376	13.92	+59.51	SABb	10.5	2.7	8.7	0.3	20.0	0.009	26	65	0.62	53
NGC 5378	13.95	+37.80	SBb	10.6	5.6	7.3	0.6	24.3	0.012	40	60	0.63	52
NGC 5406	14.01	+38.92	SBb	11.3	8.9	9.8	0.6	19.0	0.019	75	68	0.88	28
NGC 5480	14.11	+50.73	SACd	10.1	2.4	8.6	0.2	19.4	0.008	26	159	0.67	48
NGC 5519	14.24	+07.52	SBb	10.8	17.8	9.2	1.8	22.1	0.027	107	89	0.71	45
NGC 5520	14.21	+50.35	SABc	9.9	2.6	-	-	-	0.008	26	66	0.57	56
NGC 5525	14.26	+14.28	SAa	11.3	9.3	-	-	-	0.021	89	23	0.59	54
NGC 5533	14.27	+35.34	SAab	11.2	11.8	10.1	2.3	20.9	0.015	53	30	0.61	53
NGC 5622	14.44	+48.56	SABc	10.2	5.5	8.4	0.5	21.7	0.015	53	-9	0.50	61
NGC 5656	14.51	+35.32	SAb	10.6	3.5	9.0	0.3	18.9	0.013	44	56	0.63	52
NGC 5657	14.51	+29.18	SBbc	10.3	6.2	9.4	0.7	20.1	0.015	57	182	0.53	59
NGC 5665	14.54	+08.08	SABc	10.2	3.7	9.0	0.5	20.5	0.009	31	158	0.84	34
NGC 5720	14.64	+50.82	SBbc	10.8	11.6	9.6	0.6	19.3	0.028	111	129	0.65	50
NGC 5732	14.68	+38.64	SABc	9.9	5.6	8.4	0.3	20.9	0.014	53	40	0.58	55

Continues on the next page

Table A1 – *Continuation*

Name	R.A.	Decl.	Morph	$\log(M_*)$	$r_{e,*}$	$\log(M_{\text{bulge}})$	$r_{e,\text{bulge}}$	μ_{bulge}	z	Dist	PA	b/a	i
(a)	(h)	(deg)	type	(M_{\odot})	(kpc)	(M_{\odot})	(kpc)	(mag/'' ²)	(j)	(Mpc)	(deg)	(m)	(deg)
NGC 5735	14.71	+28.73	SBbc	10.4	6.8	8.5	0.3	20.6	0.015	53	87	0.83	34
NGC 5772	14.86	+40.60	SAab	11.0	8.5	9.7	0.6	19.1	0.018	71	39	0.57	56
NGC 5888	15.22	+41.26	SBb	11.2	10.8	9.7	1.0	20.1	0.031	125	158	0.54	58
NGC 5957	15.59	+12.05	SBb	10.3	3.7	8.6	0.4	20.6	0.008	26	89	0.75	42
NGC 5971	15.59	+56.46	SABb	10.3	5.6	9.4	2.8	22.7	0.016	48	128	0.49	61
NGC 6004	15.84	+18.94	SBbc	10.7	6.6	8.7	0.2	19.1	0.015	53	73	0.94	20
NGC 6063	16.12	+07.98	SAbc	10.1	5.2	7.5	0.3	22.5	0.011	39	152	0.60	53
NGC 6154	16.43	+49.84	SBab	10.9	9.0	9.7	1.0	20.4	0.022	88	134	0.65	50
NGC 6155	16.44	+48.37	SAc	10.1	2.9	8.4	0.2	19.5	0.010	35	149	0.68	47
NGC 6301	17.14	+42.34	SAbc	11.0	15.1	9.1	0.7	21.0	0.029	120	109	0.60	54
NGC 6314	17.21	+23.27	SAab	11.2	8.8	10.5	1.5	19.4	0.024	97	176	0.51	60
NGC 6941	20.61	-04.62	SBb	10.9	11.6	9.6	0.8	20.0	0.022	89	122	0.73	44
NGC 7311	22.57	+05.57	SAA	11.1	5.7	10.1	0.7	18.7	0.015	66	13	0.49	61
NGC 7321	22.61	+21.62	SBbc	10.9	9.6	9.5	0.4	18.6	0.024	102	31	0.69	47
NGC 7364	22.74	-00.16	SAab	10.9	6.0	10.5	6.3	22.2	0.016	71	65	0.65	50
NGC 7466	23.03	+27.05	SAbc	10.8	12.3	9.4	1.8	21.6	0.025	107	201	0.53	59
NGC 7489	23.13	+23.00	SAbc	10.5	10.6	-	-	-	0.021	89	165	0.55	58
NGC 7549	23.25	+19.04	SBbc	10.6	8.8	10.0	2.8	21.8	0.016	66	140	0.75	42
NGC 7591	23.30	+06.59	SBbc	10.8	8.4	10.0	1.8	20.9	0.016	71	160	0.59	55
NGC 7631	23.36	+08.22	SAb	10.5	7.0	9.3	3.0	23.1	0.013	53	76	0.44	65
NGC 7653	23.41	+15.28	SAb	10.5	6.3	9.4	1.5	21.4	0.014	62	163	0.88	28
NGC 7716	23.61	+00.30	SAb	10.4	4.2	9.3	0.3	18.5	0.009	35	27	0.71	45
NGC 7722	23.64	+15.95	SAab	11.2	9.1	10.1	1.4	20.1	0.013	57	144	0.87	29
NGC 7782	23.90	+07.97	SAb	11.1	10.7	9.7	0.8	19.9	0.018	75	178	0.55	57
NGC 7787	23.94	+00.55	SABab	10.6	8.8	9.4	2.3	22.5	0.022	97	3	0.63	51
NGC 7819	00.07	+31.47	SAc	10.4	8.4	9.6	0.8	20.0	0.016	71	87	0.53	59
NGC 7824	00.09	+06.92	SAab	11.2	11.9	10.2	1.5	19.9	0.020	88	160	0.75	42
UGC 00005	00.05	-01.91	SAbc	10.8	10.0	8.9	0.5	20.6	0.024	106	235	0.54	58
UGC 00036	00.09	+06.77	SABab	11.0	8.7	9.4	0.5	19.4	0.021	89	9	0.60	54
UGC 01918	02.46	+25.67	SBb	10.7	8.0	8.9	0.3	19.5	0.017	71	-60	0.54	58
UGC 02311	02.82	-00.87	SBbc	10.7	8.2	9.7	0.6	19.0	0.023	102	43	0.55	58
UGC 02443	02.97	-02.04	SAcd	9.6	3.4	7.3	0.3	22.6	0.008	35	-16	0.55	58
UGC 03944	07.64	+37.63	SABbc	10.0	5.6	-	-	-	0.014	53	-56	0.49	62
UGC 03973	07.71	+49.81	SBbc	10.8	7.7	9.5	0.3	17.0	0.023	97	105	0.54	58
UGC 03995	07.74	+29.25	SBb	10.9	12.8	9.6	0.7	19.7	0.016	66	103	0.46	64
UGC 04145	07.99	+15.39	SABa	11.0	7.6	10.1	0.5	17.8	0.016	88	133	0.47	63
UGC 04195	08.09	+66.78	SBb	10.5	7.8	8.9	0.4	20.2	0.017	71	112	0.62	53
UGC 04262	08.32	+83.27	SABbc	10.6	11.6	9.6	1.0	20.4	0.020	80	154	0.71	46
UGC 04308	08.29	+21.69	SBc	10.3	6.0	8.5	0.3	19.8	0.013	48	111	0.76	41
UGC 05108	09.59	+29.81	SBb	10.9	17.2	-	-	-	0.028	116	135	0.77	40
UGC 05520	10.25	+65.14	SBcd	9.8	5.7	9.5	0.9	20.6	0.012	52	99	0.48	62
UGC 06312	11.30	+07.84	SAab	11.0	13.2	10.2	1.7	20.3	0.023	93	48	0.45	64
UGC 07012	12.03	+29.85	SABcd	9.4	4.5	8.6	0.7	22.0	0.012	44	13	0.54	58
UGC 08733	13.81	+43.41	SBdm	9.4	4.5	-	-	-	0.010	31	187	0.49	61
UGC 08781	13.87	+21.54	SBb	11.1	16.6	9.8	0.9	19.8	0.027	111	171	0.52	59

Continues on the next page

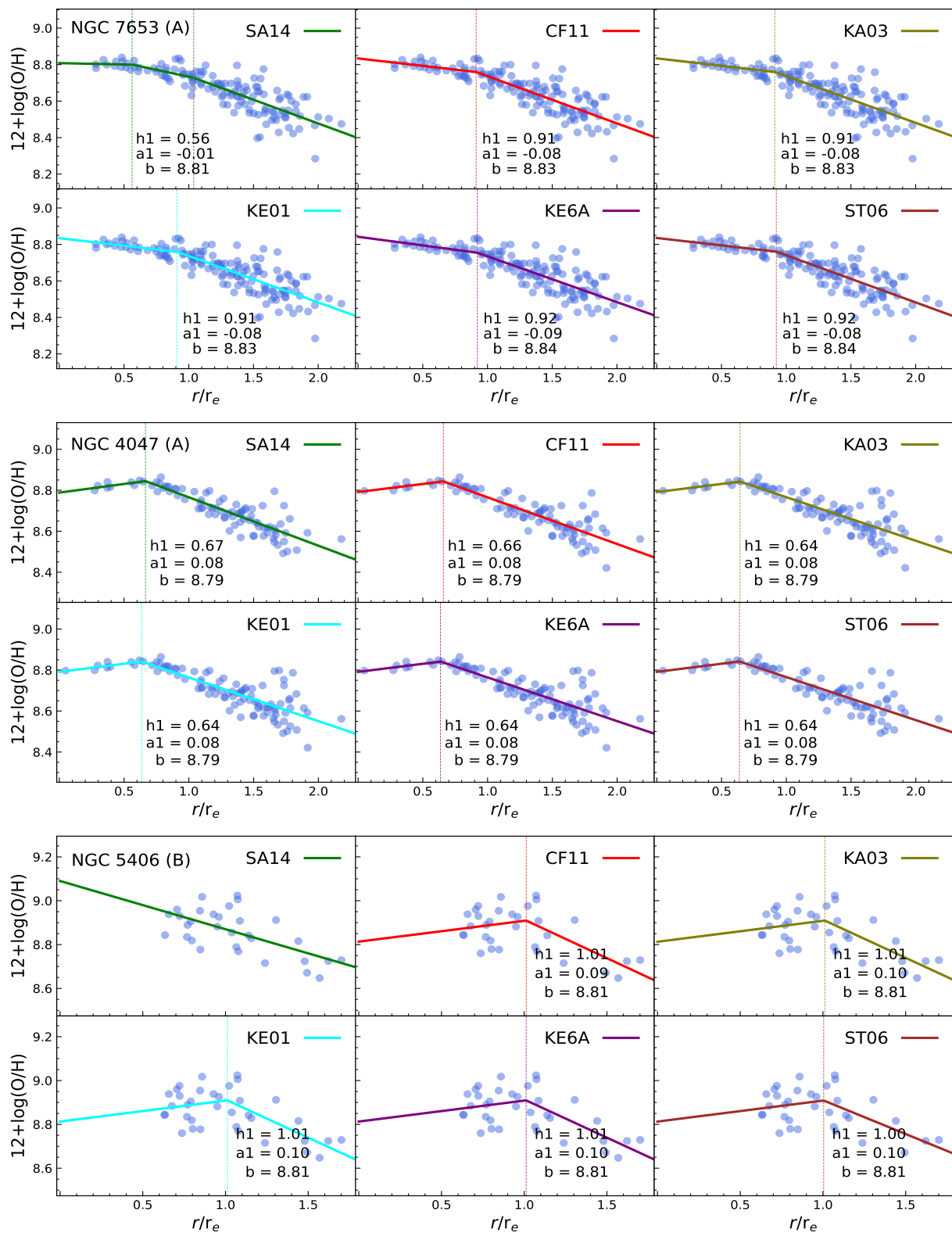
Table A1 – *Continuation*

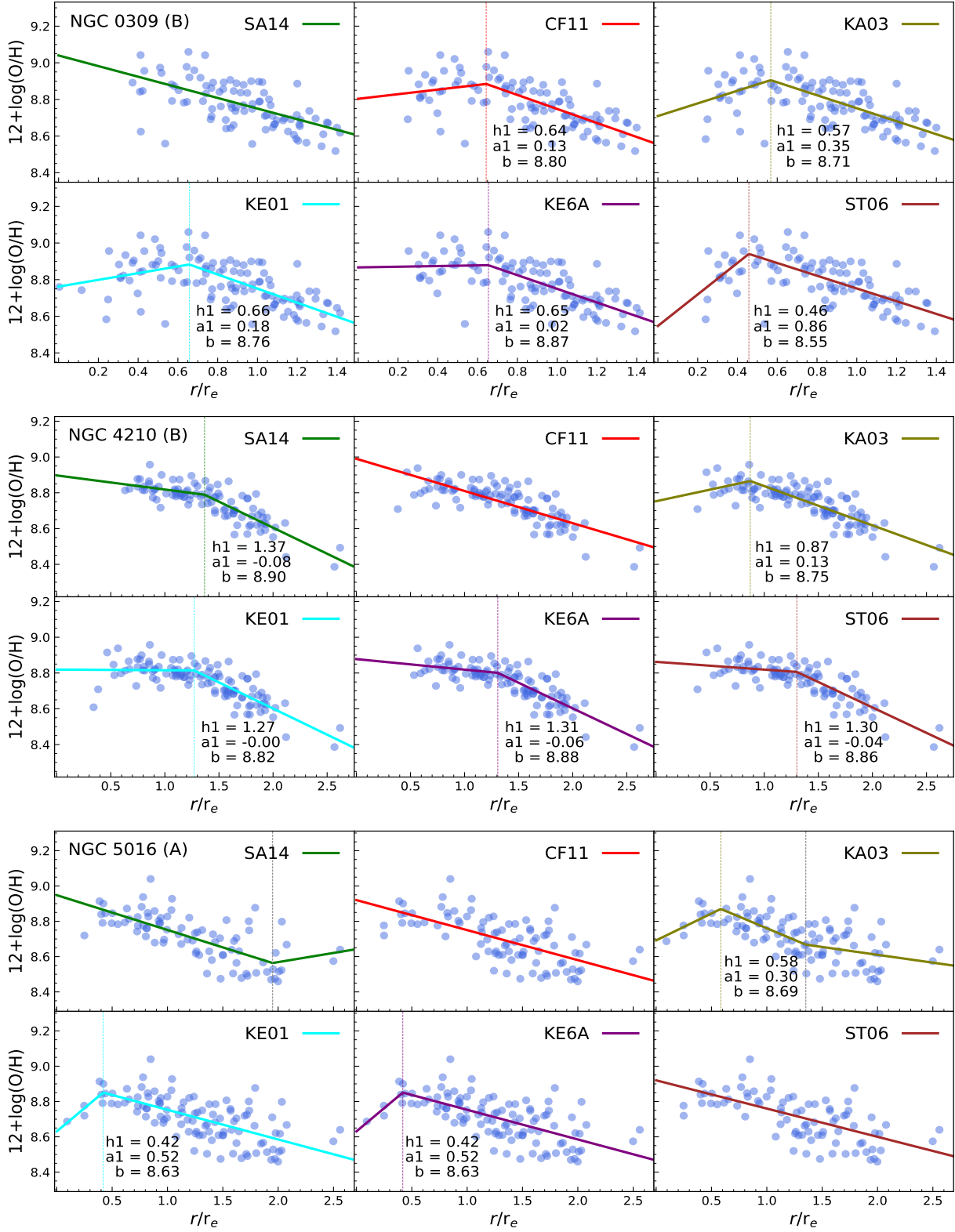
Name	R.A.	Decl.	Morph	$\log(M_*)$	$r_{e,*}$	$\log(M_{\text{bulge}})$	$r_{e,\text{bulge}}$	μ_{bulge}	z	Dist	PA	b/a	i	
(a)	(h)	(deg)	type	(M_{\odot})	(kpc)	(M_{\odot})	(kpc)	(mag/'' ²)	(j)	(Mpc)	(deg)	(l)	(m)	(n)
UGC 09110	14.24	+15.62	SABb	10.2	9.0	9.2	0.3	18.7	0.018	76	21	0.45	64	
UGC 09291	14.48	+39.00	SACd	10.3	6.1	7.8	0.4	22.4	0.012	39	107	0.52	59	
UGC 09476	14.69	+44.51	SABc	10.2	4.7	8.4	0.4	21.1	0.013	44	117	0.63	51	
UGC 09777	15.24	+20.48	SABc	10.3	6.7	9.0	1.5	22.6	0.018	66	145	0.60	54	
UGC 09842	15.42	+37.96	SBbc	10.7	13.7	9.6	2.8	22.8	0.032	129	-12	0.50	61	
UGC 10796	17.28	+61.92	SABcd	9.4	4.8	9.3	2.1	22.5	0.012	44	114	0.49	62	
UGC 11649	20.92	-01.23	SBab	10.6	5.7	9.0	0.7	20.9	0.013	53	94	0.88	29	
UGC 11680NED01	21.13	+03.87	SBb	11.1	14.0	-	-	-	0.026	113	101	0.77	40	
UGC 12185	22.79	+31.37	SBb	10.7	8.2	9.3	0.7	20.1	0.022	93	145	0.47	63	
UGC 12224	22.88	+06.09	SAC	10.1	7.5	8.6	0.5	21.1	0.012	48	31	0.83	34	
UGC 12633	23.50	+15.76	SABab	10.3	6.8	-	-	-	0.014	57	146	0.69	47	
UGC 12767	23.75	+07.04	SBb	11.0	12.3	-	-	-	0.017	75	34	0.87	29	
UGC 12816	23.86	+03.08	SAC	9.8	8.6	9.6	2.6	22.6	0.018	75	145	0.62	52	

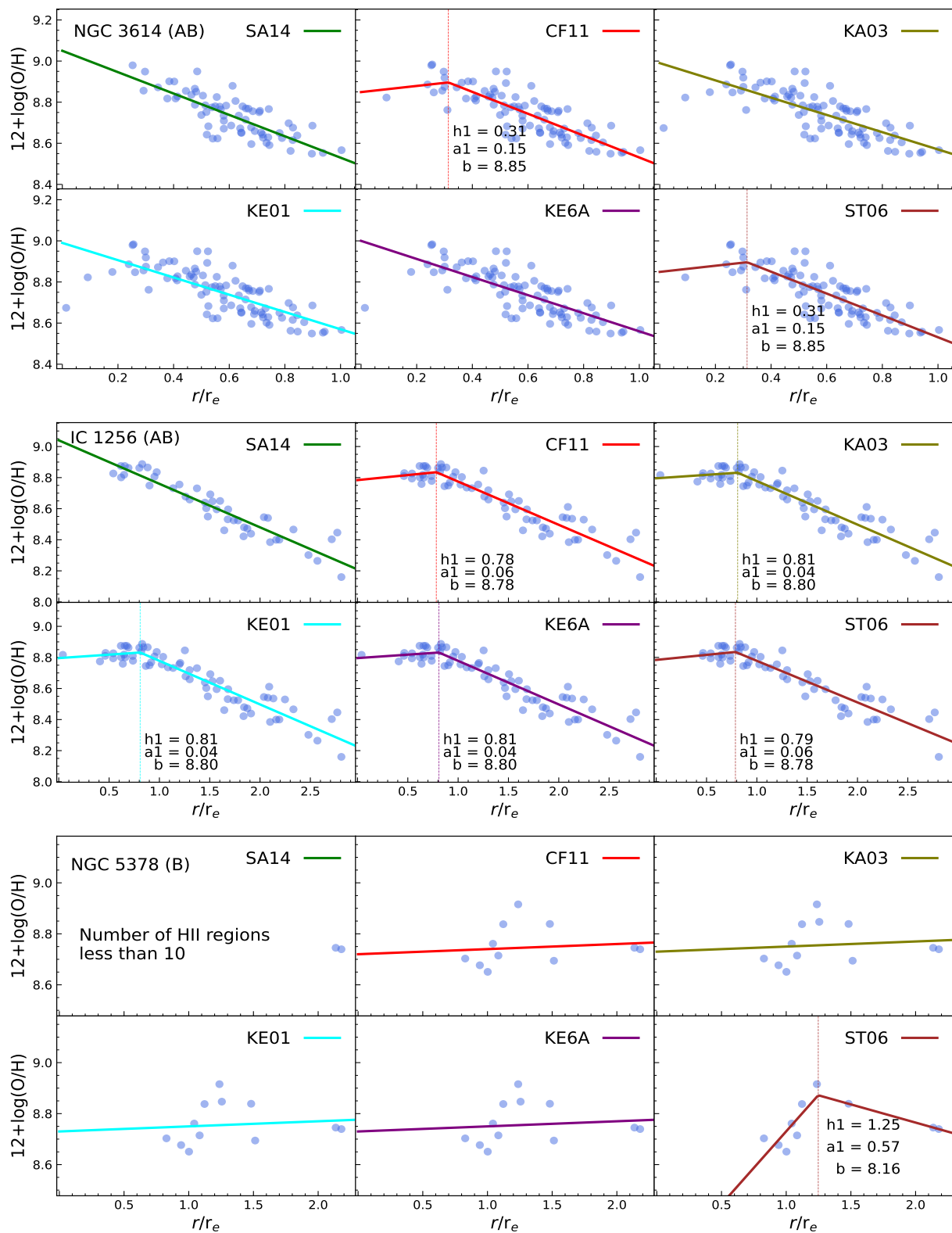
End of the table

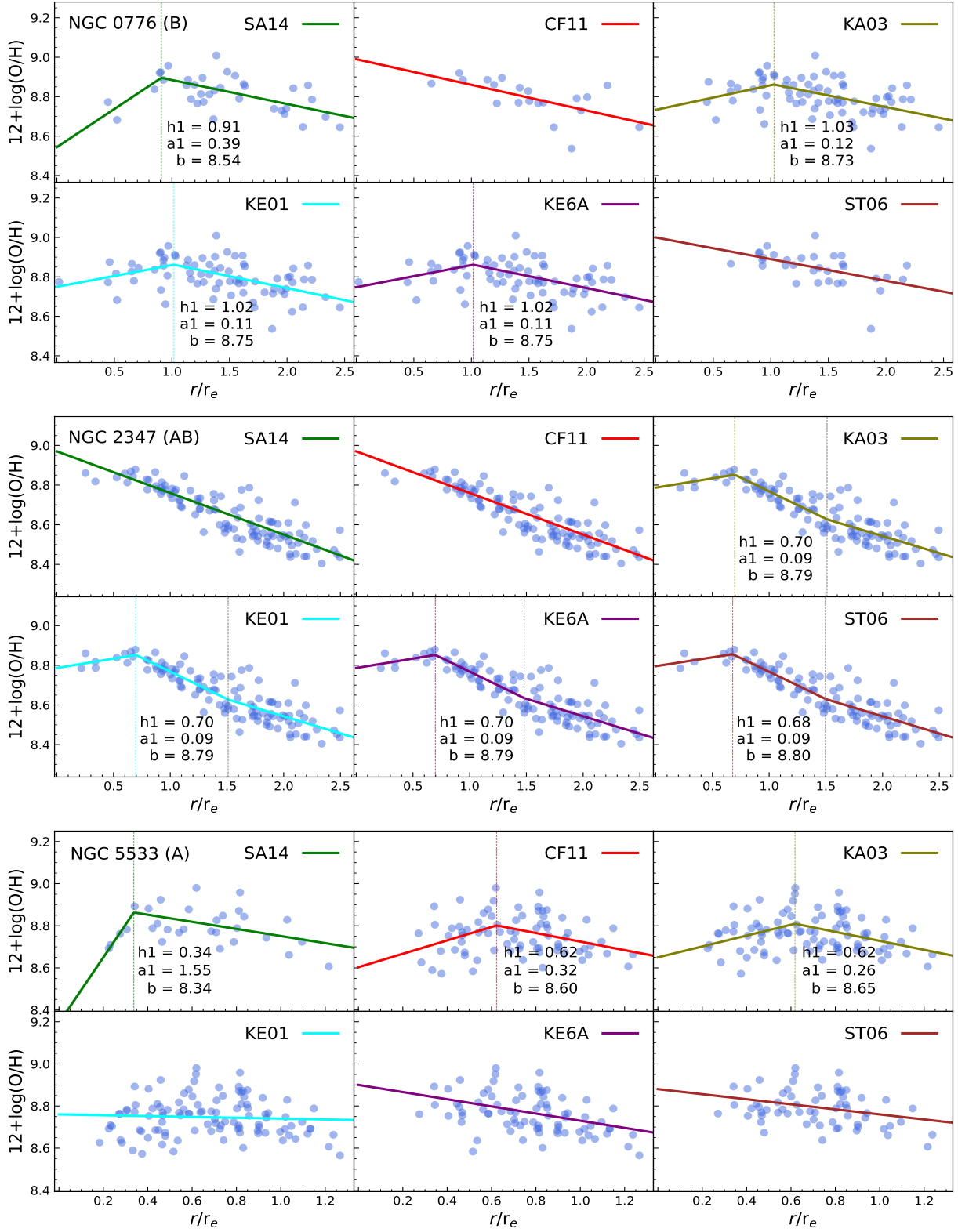
B. PROFILES OF ABUNDANCE GRADIENTS WITHOUT DIG CONTAMINATION

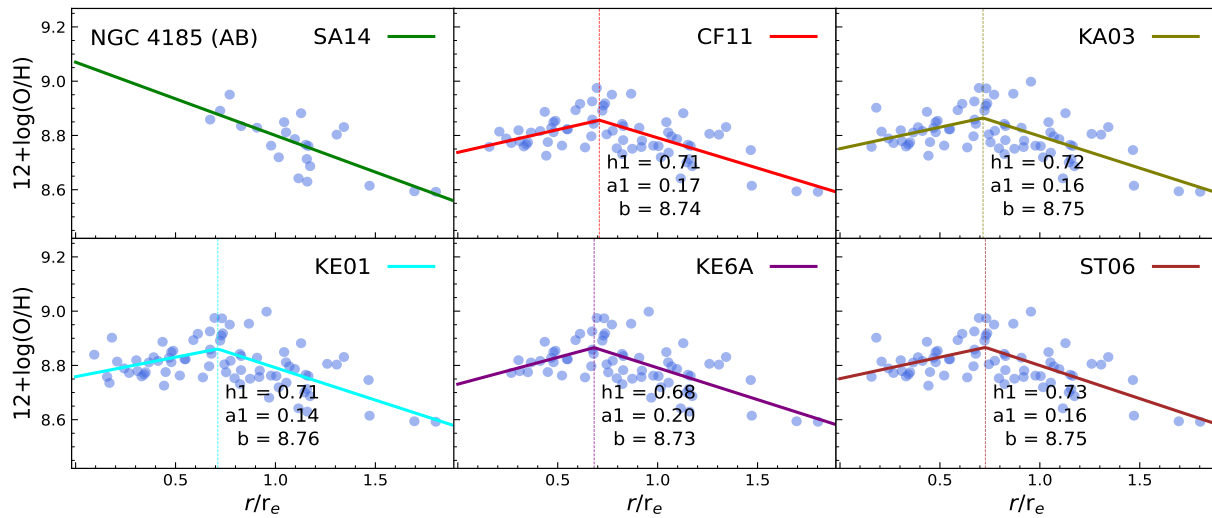
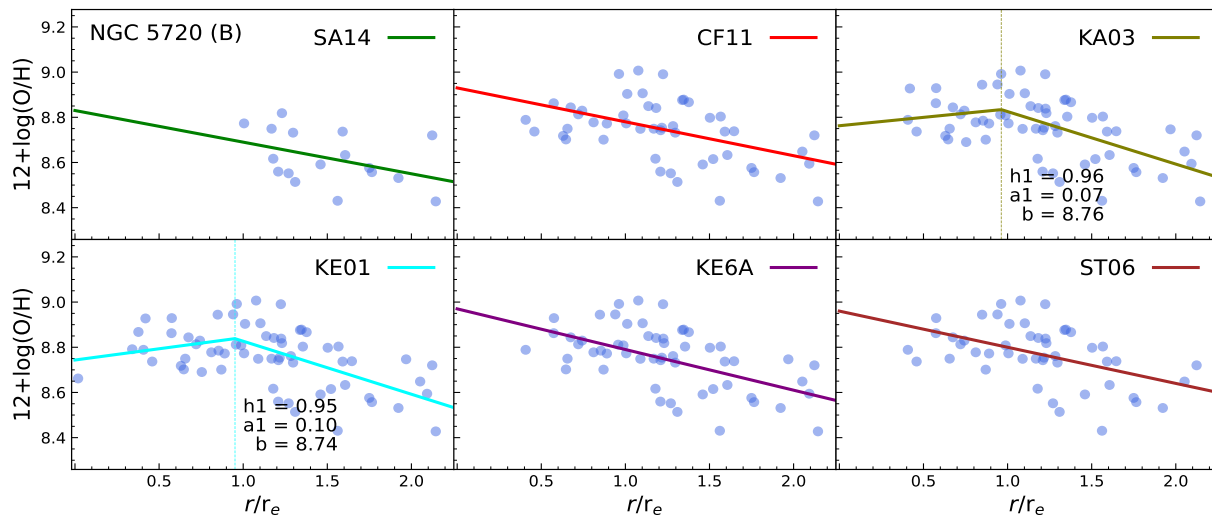
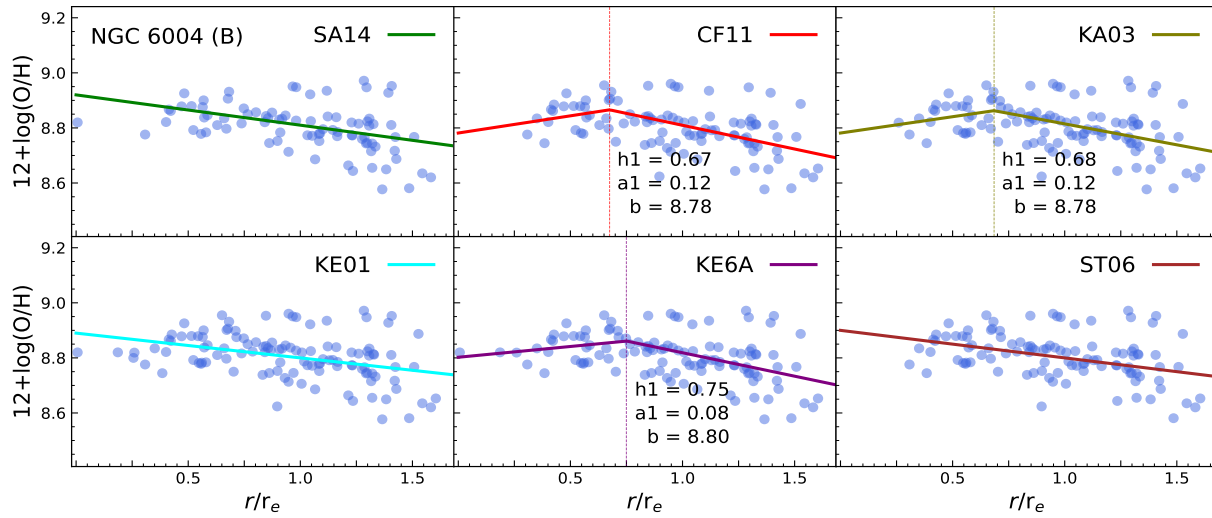
In this appendix, we present graphs with fits of the oxygen abundance gradients for the 32 galaxies that exhibited an inner drop in at least one of the six HII region selection criteria adopted in this study, after DIG decontamination. An exception is NGC 5378, excluded from the sample by the criterion of [Sánchez et al. \(2014\)](#) due to having fewer than 10 HII regions, resulting in the absence of a fitted profile for this criterion.

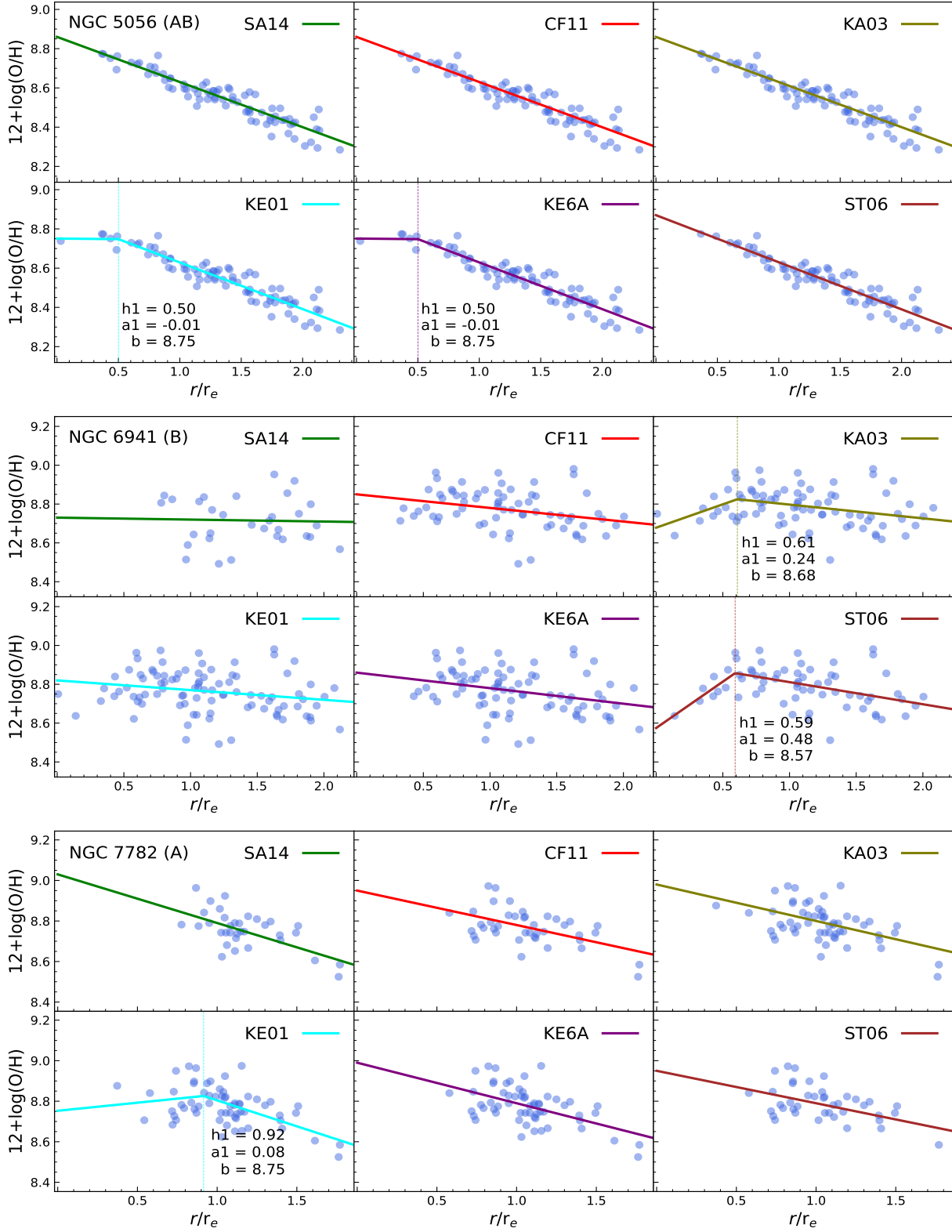


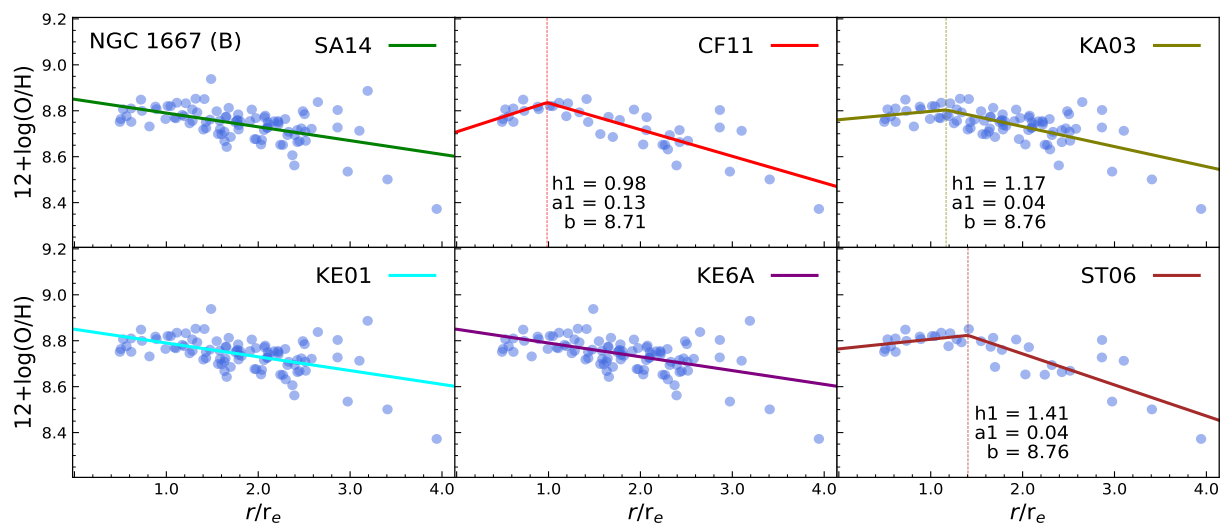
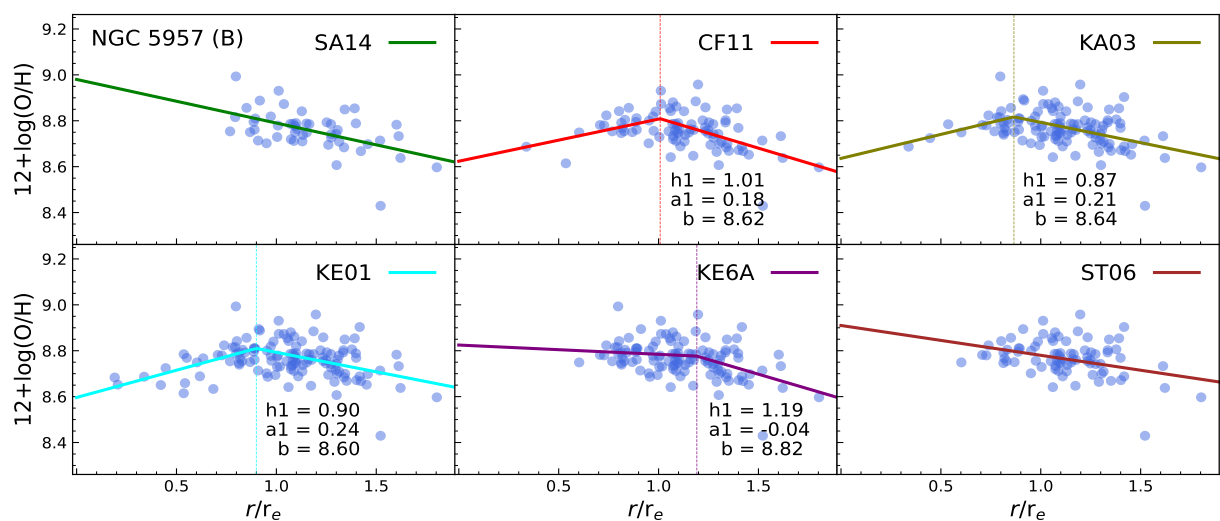
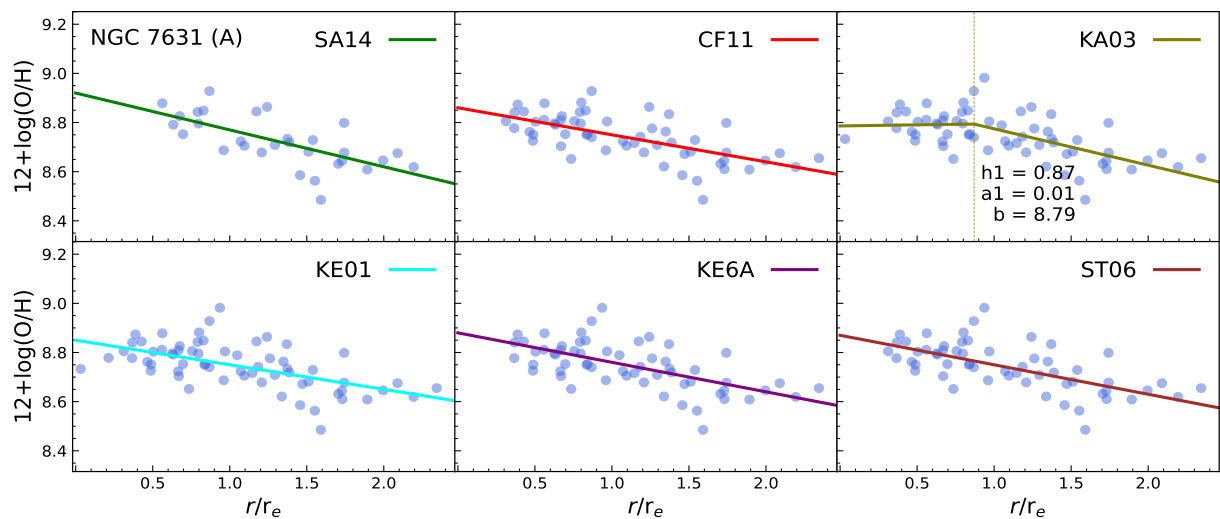


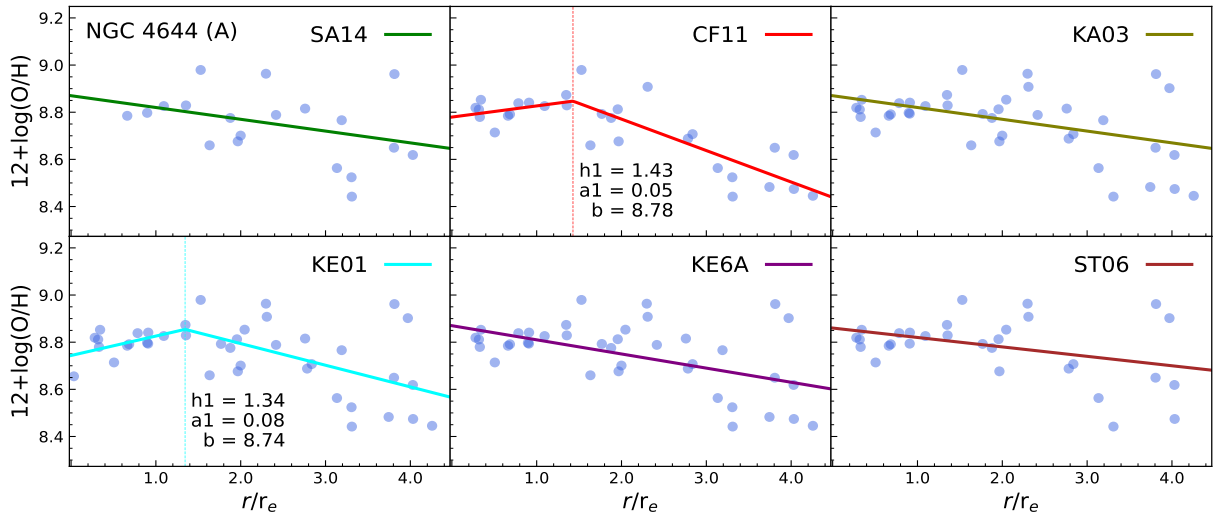
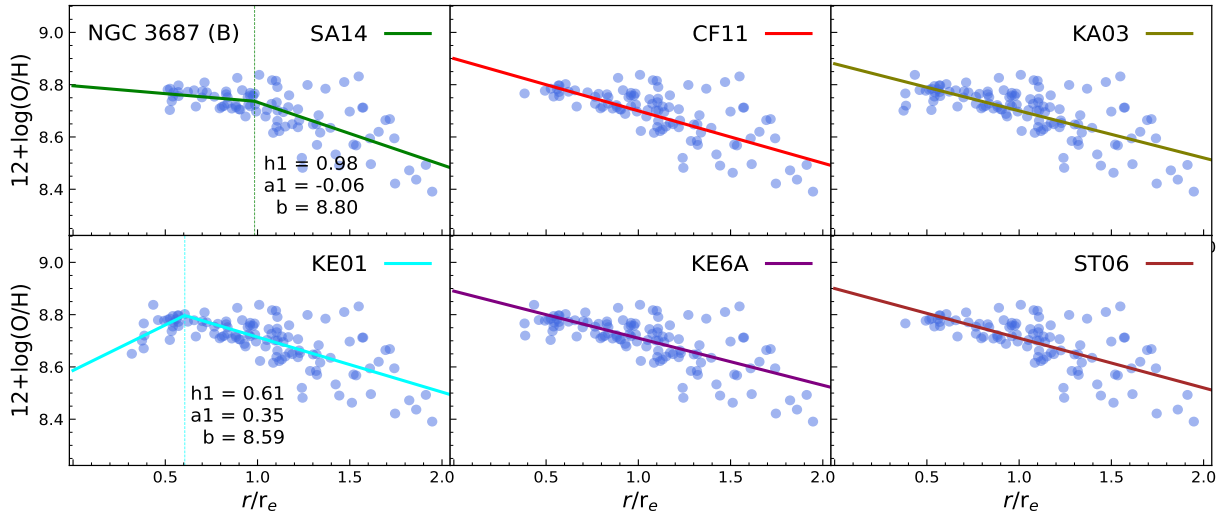
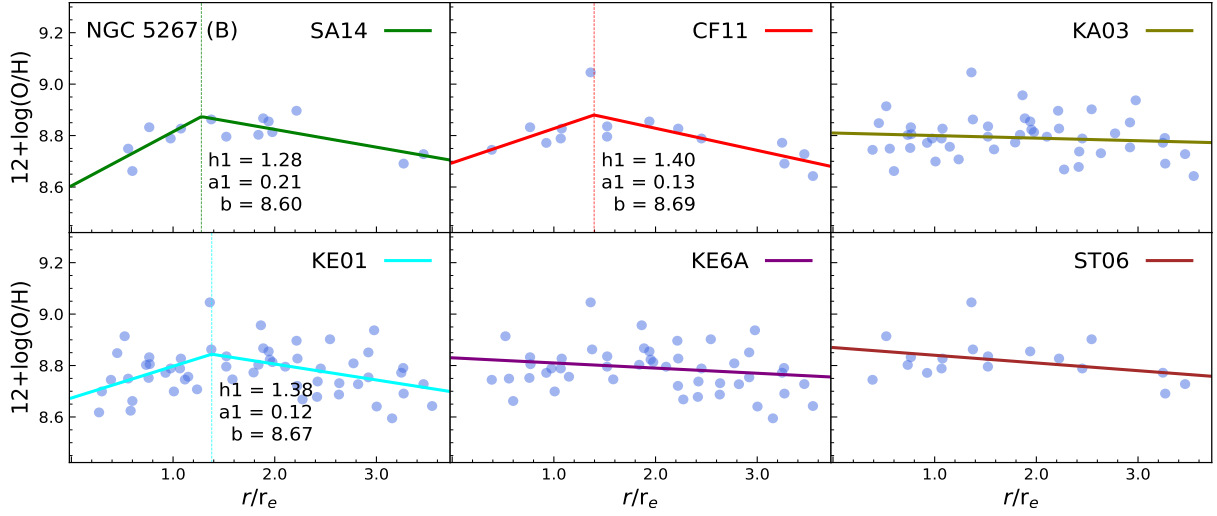


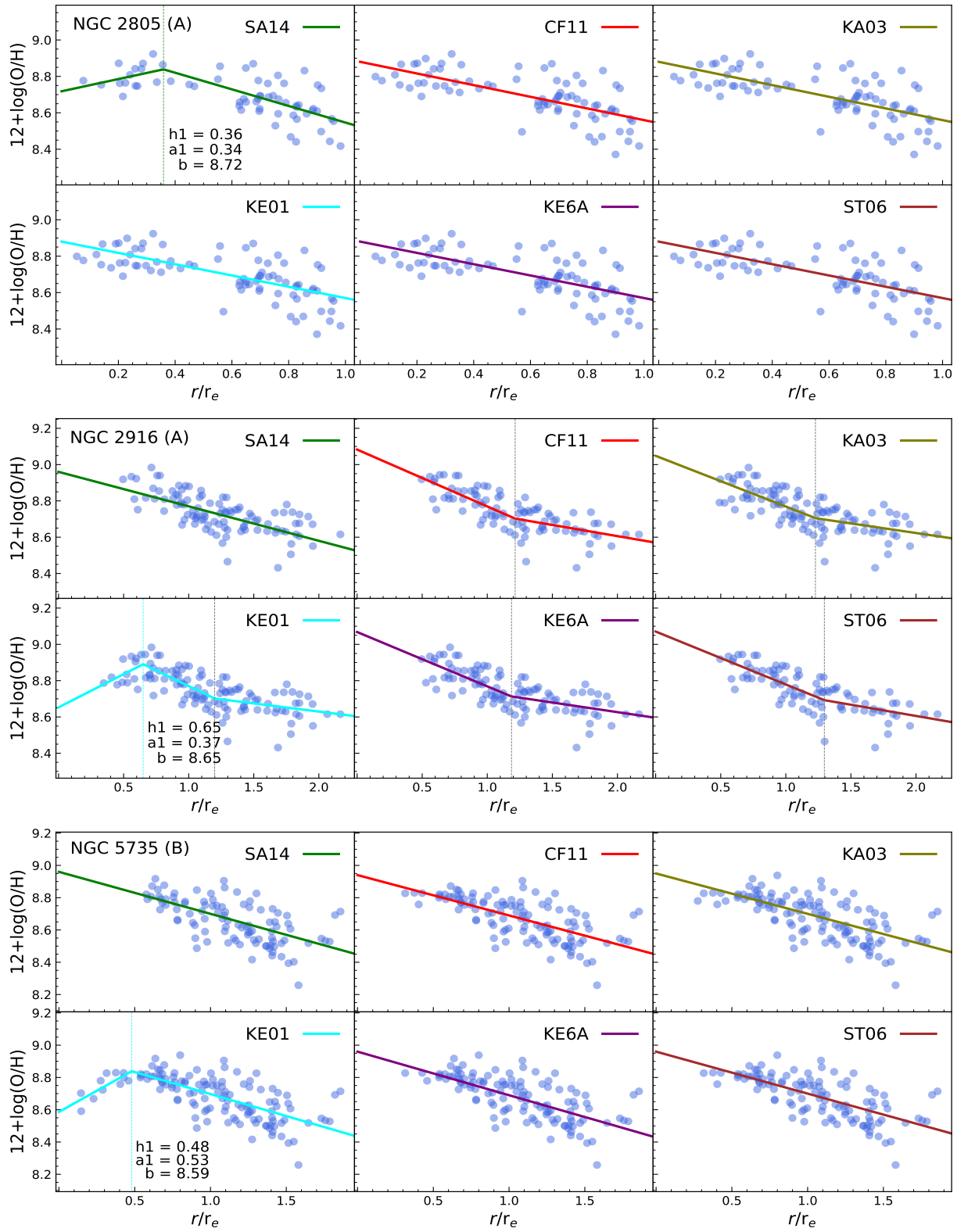


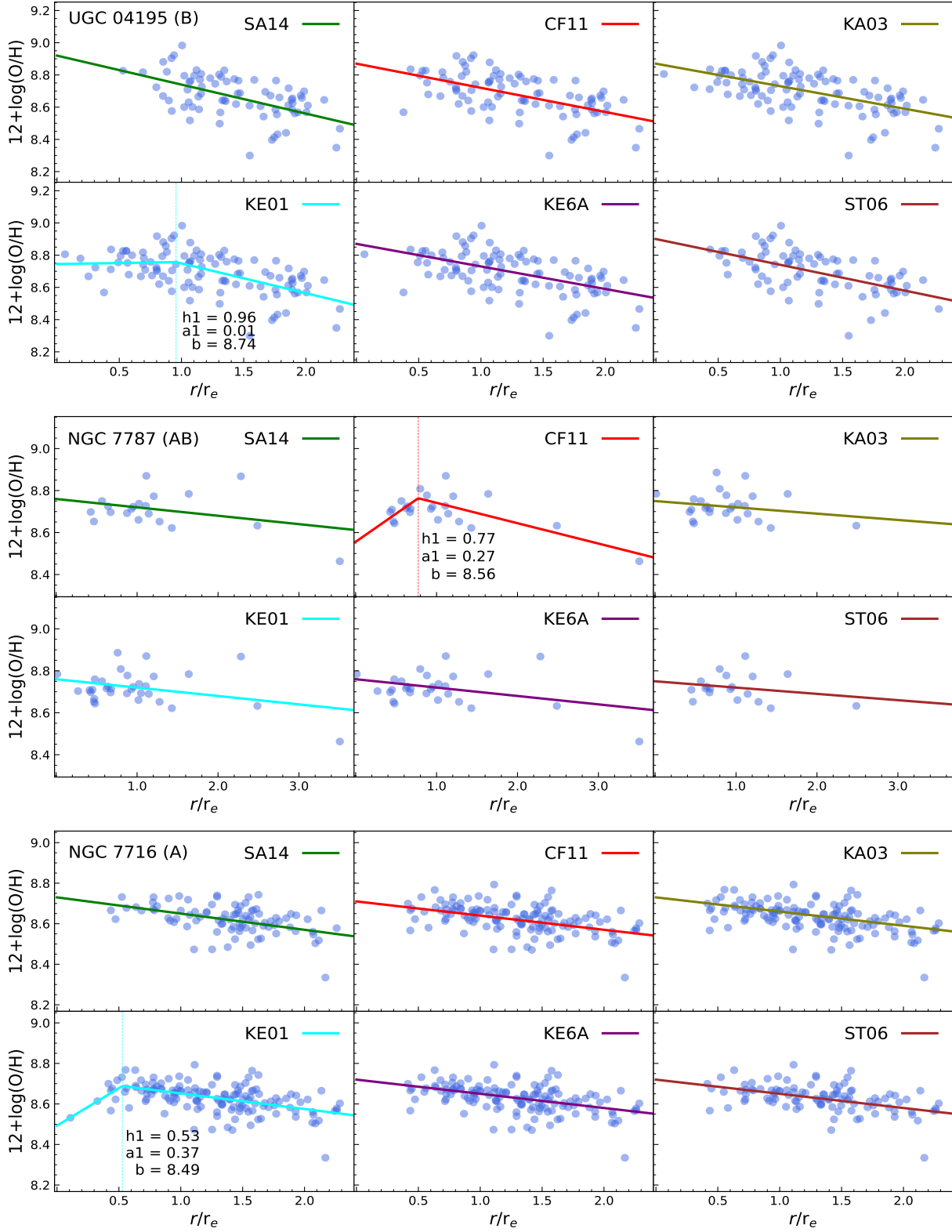


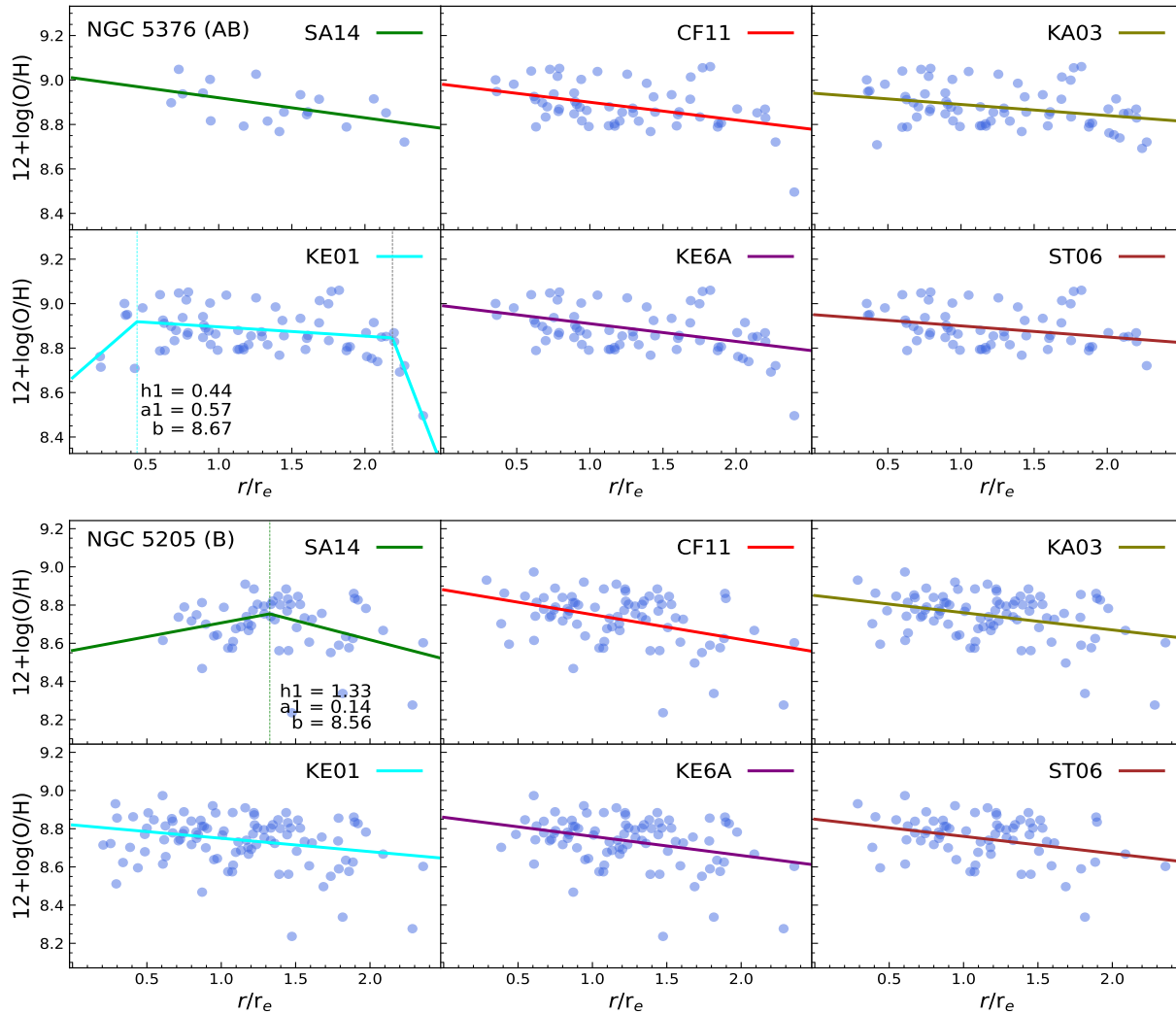












REFERENCES

- Akaike, H. 1973, Akadémiai Kiadó, Budapest
- Aller, L. H. 1984, Physics of thermal gaseous nebulae, Vol. 112 (Springer Dordrecht (Dordrecht, Holland: D. Reidel Publishing Company)),
doi: <https://doi.org/10.1007/978-94-010-9639-3>
- Alloin, D., Collin-Souffrin, S., Joly, M., & Vigroux, L. 1979, A&A, 78, 200
- Andrae, R. 2010, arXiv e-prints, 1009.2755,
doi: [10.48550/arXiv.1009.2755](https://doi.org/10.48550/arXiv.1009.2755)
- Baldwin, J. A., Phillips, M. M., & Terlevich, R. 1981, PASP, 93, 5, doi: [10.1086/130766](https://doi.org/10.1086/130766)
- Belfiore, A., Courteau, S., Corsini, E. M., & Zhu, Y. 2012, MNRAS, 419, 2497,
doi: [10.1111/j.1365-2966.2011.19903.x](https://doi.org/10.1111/j.1365-2966.2011.19903.x)
- Belfiore, F., Maiolino, R., Bundy, K., et al. 2015, MNRAS, 449, 867, doi: [10.1093/mnras/stv296](https://doi.org/10.1093/mnras/stv296)
- Belfiore, F., Santoro, F., Groves, B., et al. 2022, A&A, 659, A26, doi: [10.1051/0004-6361/202141859](https://doi.org/10.1051/0004-6361/202141859)
- Belley, J., & Roy, J. R. 1992, ApJS, 78, 61,
doi: [10.1086/191621](https://doi.org/10.1086/191621)
- Berg, D. A., Pogge, R. W., Skillman, E. D., et al. 2020, ApJ, 893, 96, doi: [10.3847/1538-4357/ab7eab](https://doi.org/10.3847/1538-4357/ab7eab)
- Bilitewski, T., & Schönrich, R. 2012, MNRAS, 426, 2266,
doi: [10.1111/j.1365-2966.2012.21827.x](https://doi.org/10.1111/j.1365-2966.2012.21827.x)
- Binney, J., & Merrifield, M. 1998, Galactic Astronomy (Princeton, NJ : Princeton University Press, 1998. (Princeton series in astrophysics))
- Bird, J. C., Kazantzidis, S., & Weinberg, D. H. 2012, MNRAS, 420, 913, doi: [10.1111/j.1365-2966.2011.19728.x](https://doi.org/10.1111/j.1365-2966.2011.19728.x)
- Bresolin, F., Gieren, W., Kudritzki, R.-P., et al. 2009a, ApJ, 700, 309, doi: [10.1088/0004-637X/700/1/309](https://doi.org/10.1088/0004-637X/700/1/309)

- Bresolin, F., Kennicutt, R. C., & Ryan-Weber, E. 2012, *ApJ*, 750, 122, doi: [10.1088/0004-637X/750/2/122](https://doi.org/10.1088/0004-637X/750/2/122)
- Bresolin, F., Ryan-Weber, E., Kennicutt, R. C., & Goddard, Q. 2009b, *ApJ*, 695, 580, doi: [10.1088/0004-637X/695/1/580](https://doi.org/10.1088/0004-637X/695/1/580)
- Cavichia, O., Costa, R. D. D., & Maciel, W. J. 2010, *RMxAA*, 46, 159, doi: [10.48550/arXiv.1003.0416](https://doi.org/10.48550/arXiv.1003.0416)
- Cavichia, O., Mollá, M., & Bazán, J. J. 2023, *MNRAS*, 520, 402, doi: [10.1093/mnras/stad097](https://doi.org/10.1093/mnras/stad097)
- Cavichia, O., Mollá, M., Costa, R. D. D., & Maciel, W. J. 2014, *MNRAS*, 437, 3688, doi: [10.1093/mnras/stt2164](https://doi.org/10.1093/mnras/stt2164)
- Cid Fernandes, R., Stasińska, G., Mateus, A., & Vale Asari, N. 2011, *MNRAS*, 413, 1687, doi: [10.1111/j.1365-2966.2011.18244.x](https://doi.org/10.1111/j.1365-2966.2011.18244.x)
- Collins, J. A., & Rand, R. J. 2001, *ApJ*, 551, 57, doi: [10.1086/320072](https://doi.org/10.1086/320072)
- Daniel, K. J., & Wyse, R. F. G. 2015, *MNRAS*, 447, 3576, doi: [10.1093/mnras/stu2683](https://doi.org/10.1093/mnras/stu2683)
- Davé, R., Finlator, K., & Oppenheimer, B. 2012, *MNRAS*, 421, 98, doi: [10.1111/j.1365-2966.2011.20148.x](https://doi.org/10.1111/j.1365-2966.2011.20148.x)
- Davé, R., Finlator, K., & Oppenheimer, B. D. 2011, *MNRAS*, 416, 1354, doi: [10.1111/j.1365-2966.2011.19132.x](https://doi.org/10.1111/j.1365-2966.2011.19132.x)
- Davison, A. C., & Hinkley, D. V. 1997, *Bootstrap Methods and their Application*, Cambridge Series in Statistical and Probabilistic Mathematics (Cambridge University Press)
- Dopita, M. A., Kewley, L. J., Sutherland, R. S., & Nicholls, D. C. 2016, *Ap&SS*, 361, 61, doi: [10.1007/s10509-016-2657-8](https://doi.org/10.1007/s10509-016-2657-8)
- Espinosa-Ponce, C., Sánchez, S. F., Morisset, C., et al. 2020, *MNRAS*, 494, doi: [10.1093/mnras/staa782](https://doi.org/10.1093/mnras/staa782)
- Esteban, C., Carigi, L., Copetti, M. V. F., et al. 2013, *MNRAS*, 433, 382, doi: [10.1093/mnras/stt730](https://doi.org/10.1093/mnras/stt730)
- Ferguson, A. M. N., & Clarke, C. J. 2001, *MNRAS*, 325, 781, doi: [10.1046/j.1365-8711.2001.04501.x](https://doi.org/10.1046/j.1365-8711.2001.04501.x)
- Fitzpatrick, E. L. 1999, *PASP*, 111, 63, doi: [10.1086/316293](https://doi.org/10.1086/316293)
- Flores-Fajardo, N., Morisset, C., Stasińska, G., & Binette, L. 2011, *MNRAS*, 415, 2182, doi: [10.1111/j.1365-2966.2011.18848.x](https://doi.org/10.1111/j.1365-2966.2011.18848.x)
- Fragkoudi, F., Athanassoula, E., & Bosma, A. 2016, *MNRAS*, 462, L41, doi: [10.1093/mnrasl/slw120](https://doi.org/10.1093/mnrasl/slw120)
- Garnett, D. R. 1998, in *Revista Mexicana de Astronomía y Astrofísica Conference Series*, Vol. 7, *Revista Mexicana de Astronomía y Astrofísica Conference Series*, ed. R. J. Dufour & S. Torres-Peimbert, 58
- Giovanelli, R., Haynes, M. P., Salzer, J. J., et al. 1994, *AJ*, 107, doi: [10.1086/117014](https://doi.org/10.1086/117014)
- Goetz, M., & Koeppen, J. 1992, *A&A*, 262, 455
- González Delgado, R. M., Cid Fernandes, R., Pérez, E., et al. 2016, *A&A*, 590, A44, doi: [10.1051/0004-6361/201628174](https://doi.org/10.1051/0004-6361/201628174)
- González Delgado, R. M., & Pérez, E. 1997, *AJ*, 108, 199, doi: [10.1086/312950](https://doi.org/10.1086/312950)
- Ho, I. T., Kudritzki, R.-P., Kewley, L. J., et al. 2015, *MNRAS*, 448, 2030, doi: [10.1093/mnras/stv067](https://doi.org/10.1093/mnras/stv067)
- Ho, L. C., Filippenko, A. V., & Sargent, W. L. W. 1997, *ApJ*, 487, 579, doi: [10.1086/304642](https://doi.org/10.1086/304642)
- Izotov, Y. I., Stasińska, G., Meynet, G., Guseva, N. G., & Thuan, T. X. 2006, *A&A*, 448, 955, doi: [10.1051/0004-6361:20053763](https://doi.org/10.1051/0004-6361:20053763)
- Kauffmann, G., Heckman, T. M., Tremonti, C., & et al. 2003, *MNRAS*, 346, 1055, doi: [10.1111/j.1365-2966.2003.07154.x](https://doi.org/10.1111/j.1365-2966.2003.07154.x)
- Kennicutt, R. C., J., Keel, W. C., & Blaha, C. A. 1989, *AJ*, 97, 1022, doi: [10.1086/115046](https://doi.org/10.1086/115046)
- Kewley, L. J., Dopita, M. A., Sutherland, R. S., Heisler, C. A., & Trevena, J. 2001, *ApJ*, 556, 121, doi: [10.1086/321545](https://doi.org/10.1086/321545)
- Kewley, L. J., & Ellison, S. L. 2008, *ApJ*, 681, 1183, doi: [10.1086/587500](https://doi.org/10.1086/587500)
- Kewley, L. J., Groves, B., Kauffmann, G., & Heckman, T. 2006, *MNRAS*, 372, 961, doi: [10.1111/j.1365-2966.2006.10859.x](https://doi.org/10.1111/j.1365-2966.2006.10859.x)
- Kormendy, J. 1977, *ApJ*, 218, 333, doi: [10.1086/155687](https://doi.org/10.1086/155687)
- Krishak, A., Dantluri, A., & Desai, S. 2020, *JCAP*, 2020, 007, doi: [10.1088/1475-7516/2020/02/007](https://doi.org/10.1088/1475-7516/2020/02/007)
- Kumari, N., Maiolino, R., Belfiore, F., & Curti, M. 2019, *MNRAS*, 485, 367, doi: [10.1093/mnras/stz366](https://doi.org/10.1093/mnras/stz366)
- Lacerda, E. A. D., Cid Fernandes, R., Couto, G. S., et al. 2018, *MNRAS*, 474, 3727, doi: [10.1093/mnras/stx3022](https://doi.org/10.1093/mnras/stx3022)
- Lacey, C. G., & Fall, S. M. 1985, *ApJ*, 290, 154, doi: [10.1086/162970](https://doi.org/10.1086/162970)
- Lopez, L. A., Krumholz, M. R., Bolatto, A. D., Prochaska, J. X., & Ramirez-Ruiz, E. 2011, *ApJ*, 731, 91, doi: [10.1088/0004-637X/731/2/91](https://doi.org/10.1088/0004-637X/731/2/91)
- López-Cobá, C., Sánchez, S. F., Lin, L., et al. 2022, *ApJ*, 939, 40, doi: [10.3847/1538-4357/ac937b](https://doi.org/10.3847/1538-4357/ac937b)
- Maiolino, R., & Mannucci, F. 2019, *A&A Rv*, 27, 3, doi: [10.1007/s00159-018-0112-2](https://doi.org/10.1007/s00159-018-0112-2)
- Marino, R. A., Rosales-Ortega, F. F., Sánchez, S. F., & et al. 2013, *A&A*, 559, doi: [10.1051/0004-6361/201321956](https://doi.org/10.1051/0004-6361/201321956)
- Martin, P., & Roy, J. R. 1994, *ApJ*, 424, 599, doi: [10.1086/173917](https://doi.org/10.1086/173917)
- Martin, P., & Roy, J. R. 1995, *ApJ*, 445, 161, doi: [10.1086/175682](https://doi.org/10.1086/175682)
- Matteucci, F., & Franco, P. 1989, *MNRAS*, 239, 885, doi: [10.1093/mnras/239.3.885](https://doi.org/10.1093/mnras/239.3.885)

- McCall, M. L., Rybski, P. M., & Shields, G. A. 1985, *ApJ*, 57, 1, doi: [10.1086/190994](https://doi.org/10.1086/190994)
- Méndez-Abreu, J., Ruiz-Lara, T., Sánchez-Menguiano, L., et al. 2017, *A&A*, 598, A32, doi: [10.1051/0004-6361/201629525](https://doi.org/10.1051/0004-6361/201629525)
- Méndez-Delgado, J. E., Amayo, A., Arellano-Córdova, K. Z., et al. 2022, *MNRAS*, 510, 4436, doi: [10.1093/mnras/stab3782](https://doi.org/10.1093/mnras/stab3782)
- Minchev, I., & Famaey, B. 2010, *ApJ*, 722, 112, doi: [10.1088/0004-637X/722/1/112](https://doi.org/10.1088/0004-637X/722/1/112)
- Mollá, M., Díaz, Á. I., Cavichia, O., et al. 2019, *MNRAS*, 482, 3071, doi: [10.1093/mnras/sty2877](https://doi.org/10.1093/mnras/sty2877)
- Muggeo, V. M. 2003, *Statist. Med.*, 22, 3055, doi: [10.1002/sim.1545](https://doi.org/10.1002/sim.1545)
- Narisetty, N. N. 2020, in *Handbook of Statistics, Vol. 43, Principles and Methods for Data Science*, ed. A. S. R. Srinivasa Rao & C. R. Rao (Elsevier), 207–248, doi: <https://doi.org/10.1016/bs.host.2019.08.001>
- Oey, M. S., Parker, J. S., Mikles, V. J., & Zhang, X. 2003, *AJ*, 126, 2317, doi: [10.1086/378163](https://doi.org/10.1086/378163)
- Oppenheimer, B. D., & Davé, R. 2008, *MNRAS*, 387, 577, doi: [10.1111/j.1365-2966.2008.13280.x](https://doi.org/10.1111/j.1365-2966.2008.13280.x)
- Oppenheimer, B. D., Davé, R., Kereš, D., et al. 2010, *MNRAS*, 406, 2325, doi: [10.1111/j.1365-2966.2010.16872.x](https://doi.org/10.1111/j.1365-2966.2010.16872.x)
- Osterbrock, D. E. 1989, *Annals of the New York Academy of Sciences*, 571, 99, doi: [10.1111/j.1749-6632.1989.tb50500.x](https://doi.org/10.1111/j.1749-6632.1989.tb50500.x)
- Osterbrock, D. E., & Ferland, G. J. 2006, *Astrophysics of gaseous nebulae and active galactic nuclei* (Sausalito, California, USA: University Science Books), 461 p.
- Pagel, B. E. J., Edmunds, M. G., Blackwell, D. E., Chun, M. S., & Smith, G. 1979, *MNRAS*, 189, 95, doi: [10.1093/mnras/189.1.95](https://doi.org/10.1093/mnras/189.1.95)
- Pagel, B. E. J., Simonson, E. A., Terlevich, R. J., & Edmunds, M. G. 1992, *MNRAS*, 255, 325, doi: [10.1093/mnras/255.2.325](https://doi.org/10.1093/mnras/255.2.325)
- Pearson, K. 1895, *Proceedings of the Royal Society of London Series I*, 58, 240
- Peimbert, M., & Costero, R. 1969, *Boletín de los Observatorios Tonantzintla y Tacubaya*, 5, 3
- Pérez-Montero, E., & Contini, T. 2009, *MNRAS*, 398, 949–960, doi: [10.1111/j.1365-2966.2009.15145.x](https://doi.org/10.1111/j.1365-2966.2009.15145.x)
- Pettini, M., & Pagel, B. E. J. 2004, *MNRAS*, 348, L59–L63, doi: [10.1111/j.1365-2966.2004.07591.x](https://doi.org/10.1111/j.1365-2966.2004.07591.x)
- Pilgrim, C. 2021, *Journal of Open Source Software*, 6, 3859, doi: [10.21105/joss.03859](https://doi.org/10.21105/joss.03859)
- Pilyugin, L. S., Grebel, E. K., Zinchenko, I. A., et al. 2018, *A&A*, 613, A1, doi: [10.1051/0004-6361/201732185](https://doi.org/10.1051/0004-6361/201732185)
- Prugniel, P., & Simien, F. 1997, *A&A*, 321, 111
- Qu, Y., Di Matteo, P., Lehnert, M. D., van Driel, W., & Jog, C. J. 2011, *A&A*, 535, A5, doi: [10.1051/0004-6361/201116502](https://doi.org/10.1051/0004-6361/201116502)
- Quillen, A. C., Minchev, I., Bland-Hawthorn, J., & Haywood, M. 2009, *MNRAS*, 397, 1599, doi: [10.1111/j.1365-2966.2009.15054.x](https://doi.org/10.1111/j.1365-2966.2009.15054.x)
- Reynolds, R. J., Sterling, N. C., Haffner, L. M., & Tufte, S. L. 2001, *ApJL*, 548, L221, doi: [10.1086/319119](https://doi.org/10.1086/319119)
- Rosales-Ortega, F. F., Díaz, A. I., Kennicutt, R. C., & Sánchez, S. F. 2011, *MNRAS*, 415, 2439, doi: [10.1111/j.1365-2966.2011.18870.x](https://doi.org/10.1111/j.1365-2966.2011.18870.x)
- Roškar, R., Debattista, V. P., Quinn, T. R., & Wadsley, J. 2012, *MNRAS*, 426, 2089, doi: [10.1111/j.1365-2966.2012.21860.x](https://doi.org/10.1111/j.1365-2966.2012.21860.x)
- Roy, J. R. 1996, in *Astronomical Society of the Pacific Conference Series, Vol. 91, IAU Colloq. 157: Barred Galaxies*, ed. R. Buta, D. A. Crocker, & B. G. Elmegreen, 63
- Sánchez, S. F. 2006, *Astronomische Nachrichten*, 327, 850, doi: [10.1002/asna.200610643](https://doi.org/10.1002/asna.200610643)
- Sánchez, S. F., Rosales-Ortega, F. F., Marino, R. A., & et al. 2012, *A&A*, 546, A2, doi: [10.1051/0004-6361/201219578](https://doi.org/10.1051/0004-6361/201219578)
- Sánchez, S. F., Pérez, E., Rosales-Ortega, F. F., et al. 2015, *A&A*, 574, A47, doi: [10.1051/0004-6361/201424873](https://doi.org/10.1051/0004-6361/201424873)
- Sani, E., Marconi, A., Hunt, L. K., & Risaliti, G. 2011, *MNRAS*, 413, 1479, doi: [10.1111/j.1365-2966.2011.18229.x](https://doi.org/10.1111/j.1365-2966.2011.18229.x)
- Scarano, S., Madsen, F. R. H., Roy, N., & Lépine, J. R. D. 2008, *MNRAS*, 386, 963–972, doi: [10.1111/j.1365-2966.2008.13079.x](https://doi.org/10.1111/j.1365-2966.2008.13079.x)
- Searle, L. 1971, *ApJ*, 168, 327, doi: [10.1086/151090](https://doi.org/10.1086/151090)
- Sellwood, J. A., & Binney, J. J. 2002, *MNRAS*, 336, 785, doi: [10.1046/j.1365-8711.2002.05806.x](https://doi.org/10.1046/j.1365-8711.2002.05806.x)
- Singh, R., van de Ven, G., Jahnke, K., et al. 2013, *A&A*, 558, A43, doi: [10.1051/0004-6361/201322062](https://doi.org/10.1051/0004-6361/201322062)
- Stasińska, G., Cid Fernandes, R., Mateus, A., Sodré, L., & Asari, N. V. 2006, *MNRAS*, 371, 972, doi: [10.1111/j.1365-2966.2006.10732.x](https://doi.org/10.1111/j.1365-2966.2006.10732.x)
- Stasińska, G., Vale Asari, N., Cid Fernandes, R., et al. 2008, *MNRAS*, 391, L29, doi: [10.1111/j.1745-3933.2008.00550.x](https://doi.org/10.1111/j.1745-3933.2008.00550.x)
- Storchi-Bergmann, T., Calzetti, D., & Kinney, A. L. 1994, *ApJ*, 429, 572, doi: [10.1086/174345](https://doi.org/10.1086/174345)
- Sánchez, S. F., García-Benito, R., Zibetti, S., & et al. 2016, *A&A*, 594, A36, doi: [10.1051/0004-6361/201628661](https://doi.org/10.1051/0004-6361/201628661)
- Sánchez, S. F., Kennicutt, R. C., de Paz, A. G., & et al. 2012, *A&A*, 538, A8, doi: [10.1051/0004-6361/201117353](https://doi.org/10.1051/0004-6361/201117353)
- Sánchez, S. F., Rosales-Ortega, F. F., Iglesias-Páramo, J., & et al. 2014, *A&A*, 563, A49, doi: [10.1051/0004-6361/201322343](https://doi.org/10.1051/0004-6361/201322343)

- Sánchez-Menguiano, L., Sánchez, S. F., Pérez, I., & et al. 2016, *A&A*, 587, A70, doi: [10.1051/0004-6361/201527450](https://doi.org/10.1051/0004-6361/201527450)
- Sánchez-Menguiano, L., Sánchez, S. F., Pérez, I., et al. 2018, *A&A*, 609, A119, doi: [10.1051/0004-6361/201731486](https://doi.org/10.1051/0004-6361/201731486)
- Vale Asari, N., Couto, G. S., Cid Fernandes, R., et al. 2019, *MNRAS*, 489, 4721, doi: [10.1093/mnras/stz2470](https://doi.org/10.1093/mnras/stz2470)
- Vila-Costas, M. B., & Edmunds, M. G. 1992, *MNRAS*, 259, 121, doi: [10.1093/mnras/259.1.121](https://doi.org/10.1093/mnras/259.1.121)
- Vilchez, J. M., & Esteban, C. 1996a, *MNRAS*, 280, 720, doi: [10.1093/mnras/280.3.720](https://doi.org/10.1093/mnras/280.3.720)
- . 1996b, *MNRAS*, 280, 720, doi: [10.1093/mnras/280.3.720](https://doi.org/10.1093/mnras/280.3.720)
- Vogt, F. P. A., Dopita, M. A., Kewley, L. J., et al. 2014, *ApJ*, 793, 127, doi: [10.1088/0004-637X/793/2/127](https://doi.org/10.1088/0004-637X/793/2/127)
- Vogt, F. P. A., Pérez, E., Dopita, M. A., Verdes-Montenegro, L., & Borthakur, S. 2017, *A&A*, 601, A61, doi: [10.1051/0004-6361/201629853](https://doi.org/10.1051/0004-6361/201629853)
- Walcher, C. J., Lamareille, F., Vergani, D., & et al. 2008, *A&A*, 491, 713, doi: [10.1051/0004-6361:200810704](https://doi.org/10.1051/0004-6361:200810704)
- Walcher, C. J., Wisotzki, L., Bekeraité, S., & et al. 2014, *A&A*, 569, A1, doi: [10.1051/0004-6361/201424198](https://doi.org/10.1051/0004-6361/201424198)
- Zaritsky, D., Kennicutt, R. C. J., & Huchra, J. P. 1994, *ApJ*, 420, 87, doi: [10.1086/173544](https://doi.org/10.1086/173544)
- Zinchenko, I. A., Just, A., Pilyugin, L. S., & Lara-Lopez, M. A. 2019, *A&A*, 623, A7, doi: [10.1051/0004-6361/201834364](https://doi.org/10.1051/0004-6361/201834364)
- Zinchenko, I. A., Pilyugin, L. S., Grebel, E. K., Sánchez, S. F., & Vilchez, J. M. 2016, *MNRAS*, 462, 2715, doi: [10.1093/mnras/stw1857](https://doi.org/10.1093/mnras/stw1857)
- Zurita, A., Florido, E., Bresolin, F., Pérez-Montero, E., & Pérez, I. 2021, *MNRAS*, 500, 2359, doi: [10.1093/mnras/staa2246](https://doi.org/10.1093/mnras/staa2246)
- Zurita, A., Rozas, M., & Beckman, J. E. 2000, *A&A*, 363, 9